Microscopic origin of the effect of substrate metallicity on interfacial free energies

Laura Scalfi, Benjamin Rotenberg

Microscopic origin of the effect of substrate metallicity on interfacial free energies

Laura Scalfi,[a] Benjamin Rotenberg*,[a,b]
[a] *Physicochimie des électrolytes et Nanosystèmes Interfaciaux, Sorbonne Université, CNRS, 4 Place Jussieu F-75005 Paris, France*
[b] *Réseau sur le Stockage Electrochimique de l'Energie (RS2E), FR CNRS 3459, 33 Rue Saint Leu 80039 Amiens Cedex, France*
* *E-mail: benjamin.rotenberg@sorbonne-universite.fr*

We investigate the effect of the metallic character of solid substrates on solid-liquid interfacial thermodynamics using molecular simulations. Building on the recent development of a semi-classical Thomas-Fermi model to tune the metallicity in classical molecular dynamics simulations, we introduce a thermodynamic integration framework to compute the evolution of the interfacial free energy as a function of the Thomas-Fermi screening length. We validate this approach against analytical results for empty capacitors and by comparing the predictions in the presence of an electrolyte with values determined from the contact angle of droplets on the surface. The general expression derived in this work highlights the role of the charge distribution within the metal. We further propose a simple model to interpret the evolution of the interfacial free energy with voltage and Thomas-Fermi length, which allows us to identify the charge correlations within the metal as the microscopic origin of the evolution of the interfacial free energy with the metallic character of the substrate. This methodology opens the door to the molecular-scale study of the effect of the metallic character of the substrate on confinement-induced transitions in ionic systems, as reported in recent Atomic Force Microscopy and Surface Force Apparatus experiments.

Significance statement The properties of solid-liquid interfaces crucially depend on the delicate balance of interactions of fluid molecules between them and with the surface atoms. Recent experiments demonstrated the dramatic effect of the metallicity of the substrate on the behavior of confined liquids. Here we develop a method to investigate the interfacial thermodynamics as a function of the screening length within the metal using molecular simulations. We demonstrate the role of charge correlations in the material on the interfacial free energy and provide a simple model to capture the effects of metallicity and voltage. Our approach opens the door to the molecular-scale study of the effect of the metallic character of the substrate on confinement-induced transitions in ionic systems.

PACS numbers:

The properties of solid-liquid interfaces crucially depend on the delicate balance of interactions of fluid molecules between them and with the surface atoms. For metallic surfaces, the possibility to impose the electric potential provides a handle to control interfacial properties, *e.g.* in electro-wetting (as measured by the contact angle, which reflects interfacial free energies) [1–3], electro-tunable friction [4–8], or electro-mechanical couplings between surfaces across liquid films [9]. The wettability of electrodes also plays a role on electrochemical reactions [10] and the surface thermodynamics of metal nanoparticles can be exploited *e.g.* to fabricate electrotunable nanoplasmonic mirrors [11]. From the theoretical point of view, thermodynamic cycles and continuum electrostatics allow, for example, understanding of the quadratic dependence of interfacial free energies with voltage.

Recent experiments have further demonstrated the dramatic effect of the metallicity of the substrate on the behavior of ionic liquids confined under the tip of an Atomic Force Microscope (AFM) [12, 13] or in a Surface Force Apparatus (SFA) [14], even in the absence of voltage. The observed capillary freezing could be rationalized by considering the polarization of the metal by the liquid, usually described in terms of image charges [15–19]. This polarization depends on the screening of the electric field within the metal and can be accounted for with the Thomas-Fermi model, which quantifies the metallic character by introducing a Thomas-Fermi screening length, l_{TF}. Despite its simplicity (it is the long wave-length and static limit of Lindhard theory of screening [20]) and the limitations of the underlying free electron gas model (*e.g.* to predict the work function of noble metals [21]), this approach already proved successful to investigate the capacitance and structure of electrode-electrolyte interfaces at the mean-field level [22, 23] and to analyze the effect of l_{TF} on the interactions between ions at the surface [24], even though analytical calculations of the resulting phase behavior remain out of reach beyond a simplified one-dimensional description [25].

In addition, such continuous approaches neglect molecular features that may play an important role on the interfacial properties, such as the discrete nature of matter (on both the solid and liquid sides), which leads to the layering of the fluid at the surface, the orientation of the solvent molecules and molecular ions, or even possible templating effects modifying the phase behavior of the fluid. Molecular simulations have therefore become an essential tool to investigate the interface between fluids and metallic surfaces. Even though *ab initio* molecular dynamics (MD), for which methods

to control the potential of electrodes are now available [26, 27], provide the most accurate description of such systems, even state-of-the-art studies of metal-electrolyte interfaces [28–32] are still limited to length and time scales rarely compatible with the computation of properties such as interfacial free energies. The development of methods allowing to impose the potential between two electrodes in classical molecular dynamics simulations [33–36] opened the way to the molecular understanding *e.g.* of aqueous and non-aqueous electrochemical cells [37–39], of water and ions on platinum surfaces [40–43] or voltage-driven transitions in ionic liquids on graphite electrodes [44, 45] (see *e.g.* Refs. 46, 47 for recent reviews). The role of image charges on the interfacial properties of aqueous solutions [48] and ionic liquids has also been examined in molecular simulations [49, 50], but the classical description remained limited to the case of ideal conductors, corresponding to a vanishing l_{TF}. For comparison, typical values of the Thomas-Fermi length are 0.5 Å for good metals such as platinum and gold, or 3.6 Å for graphite [12]. We have recently extended the constant-potential method to tune the metallicity in classical molecular simulations based on the Thomas-Fermi model [51] and an alternative approach to account for screening within the metal with mobile charges has also been proposed in Ref. 52. However direct computation of interfacial free energies for each l_{TF} remains a great challenge.

Here, we investigate the influence of metallicity on interfacial free energies using molecular simulations. After a preliminary discussion of contact angles on an insulating or metallic graphite surface, we introduce the relevant thermodynamic quantities to measure the effects of metallicity and voltage. We then present a thermodynamic integration method to efficiently compute the evolution of interfacial free energies with the Thomas-Fermi screening length l_{TF} and with voltage. We provide results for empty capacitors and full electrochemical cells consisting of an aqueous electrolyte between graphite or gold electrodes. We finally explain the microscopic origin of the effect of metallicity by analyzing the charge correlations within the metal.

Contact angle on insulating or metallic surfaces

We first illustrate the influence of the metallic character of the substrate on interfacial free energies by considering the contact angle of droplets of a 1M aqueous NaCl solution on graphite. The two limits of insulating or perfectly metallic substrates, corresponding to infinite and vanishing Thomas-Fermi length l_{TF}, respectively (resp.), are modeled, all other things being equal, with fixed neutral charges or fluctuating charges determined on-the-fly in order to satisfy a constant-potential condition of the carbon atoms (see *SI Appendix*). The system is shown in the metallic case in Figs. 1a and 1b. The contact angle is determined from the equilibrium shape of the droplet, using a fit of the liquid-vapor interface by a spherical cap (see Fig. 1c).

In order to facilitate the comparison between the insulating and metallic cases, panels 1d and 1e report the corresponding one-dimensional density profiles as a function of the height z and radial distance to the droplet center of mass r. Apart from the layered structure at the interface, the simulation results (solid lines) are very well described by a homogeneous spherical cap (dashed lines – see *SI Appendix* for details). There is a significant (even though small) effect of the metallic character of the substrate on the shape of the droplet. The contact angle is determined from the intersection of the spherical cap with the solid-liquid interface, taken as the plane of the first maximum in the water density profile. This leads to $\theta(l_{TF} = 0) = 74.6 \pm 0.3°$ and $\theta(l_{TF} \to \infty) = 79.6 \pm 0.3°$. The metallic surface therefore behaves as more hydrophilic than the insulating one. The link with interfacial free energies is provided by the Young equation

$$\cos\theta(l_{TF}) = \frac{\gamma_{SV}(l_{TF}) - \gamma_{SL}(l_{TF})}{\gamma_{LV}} \,, \tag{1}$$

where γ_{SV}, γ_{SL} and γ_{LV} are the solid/vapor, solid/liquid and liquid/vapor surface tensions, respectively. By introducing the difference $\Delta\gamma_{SL}(l_{TF}) = \gamma_{SL}(l_{TF}) - \gamma_{SL}(0)$ in the solid-liquid interfacial free energy per unit area for a finite l_{TF} with respect to a perfect conductor ($l_{TF} = 0$), and similarly $\Delta\gamma_{SV}(l_{TF})$ for the solid-vapor interface and $\Delta\cos\theta(l_{TF})$ for the contact angle, we obtain

$$\Delta\gamma_{SL}(l_{TF}) - \Delta\gamma_{SV}(l_{TF}) = -\gamma_{LV}\Delta\cos\theta(l_{TF}) \,. \tag{2}$$

The value of γ_{LV} is obtained from the normal and tangential components of the pressure tensor, p_N and p_T, in a simulation of a slab of electrolyte in vacuum with a box length L_z in the direction perpendicular to the interfaces, as $\gamma_{LV} = (p_N - p_T)L_z/2 = 62.7 \pm 0.6$ mN m^{-1}. Together with $\Delta\cos\theta(\infty) = -0.09 \pm 0.01$, this leads to an excess free energy per unit area $\Delta\gamma_{SL}(\infty) - \Delta\gamma_{SV}(\infty) = 5.4 \pm 0.6$ mN m^{-1} of the insulating surface with respect to the perfectly metallic one. Note that the change in contact angle, for a given value of the free energy difference (*i.e.* $\Delta\cos\theta$), would be larger if the angle θ itself were less close to 90°. Another important aspect of metallic surfaces is the possibility to tune the interfacial tension by applying voltage, as discussed below – opening the way to more dramatic effects such as electrowetting.

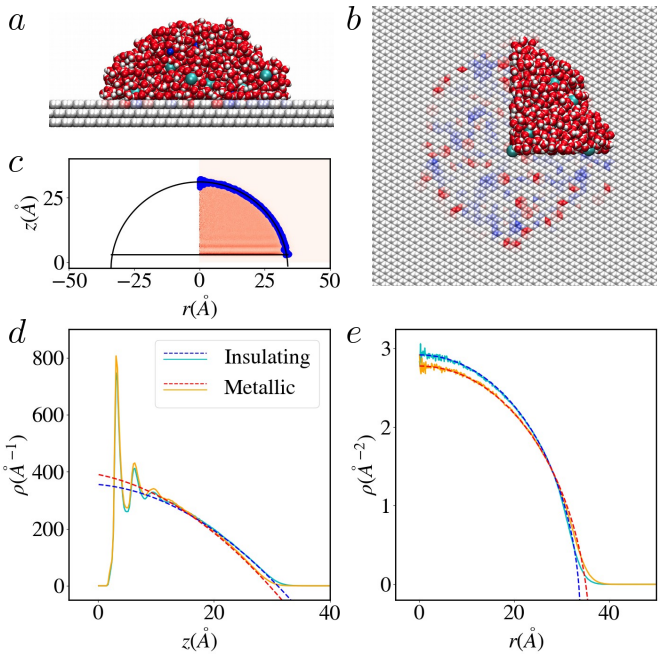

FIG. 1: Contact angles of aqueous NaCl solution droplets on graphite. Side (a) and top (b) views of the simulated system. In (b), only a quarter of the liquid is shown in order to visualize the instantaneous charges (red for negative and blue for positive) of the carbon atoms in the metallic case. (c) Two-dimensional density map as a function of the height z and the radial dimension r; the blue points locate the position of the liquid-vapor interface, fitted to a circle (solid black line) to determine the contact angle. The corresponding one-dimensional density profiles as a function of the height z and radial distance to the droplet center of mass r are shown in panels (d) and (e). In both panels, solid (resp. dashed) lines are the simulation results (resp. predictions for a homogeneous sphere), for the insulating (solid cyan, dashed blue) and metallic (solid orange, dashed red) systems.

Interfacial free energies vs metallicity and voltage

We now turn to the more direct and systematic study of the effect of metallicity and voltage on interfacial free energies. We consider capacitors consisting of two electrodes characterized by the same l_{TF} and maintained at fixed voltage $\Delta\Psi$, separated either by vacuum or by an electrolyte (see Fig. 2 a and d), in order to estimate free energy differences corresponding to solid-vapor (SV) or solid-liquid (SL) interfaces, respectively. For a capacitor characterized by a voltage-independent capacitance, the accumulated charge at a fixed voltage $\Delta\Psi$ between the electrodes is $Q = C\mathcal{A}\Delta\Psi$, with C the capacitance per unit area and $\mathcal{A}$ the electrode surface area, and the energy stored upon charging is $\Delta U = \frac{Q\Delta\Psi}{2} = \frac{C\mathcal{A}\Delta\Psi^2}{2}$. Taking into account the reversible work $-Q\Delta\Psi$ performed on the system, this provides the free energy change per unit area associated with the charge of a given capacitor

$$\frac{F_{SX}^{\Delta\Psi}(l_{TF}) - F_{SX}^{0}(l_{TF})}{\mathcal{A}} = -\frac{C_{SX}(l_{TF})}{2}\Delta\Psi^2 \,, \tag{3}$$

with $X = L, V$ and $C_{SX}(l_{TF})$ the corresponding capacitance per unit area. One can also consider the difference, for fixed $\Delta\Psi$, between perfectly metallic electrodes and electrodes characterized by a finite l_{TF}

$$\Delta F_{SX}^{\Delta\Psi}(l_{TF}) = F_{SX}^{\Delta\Psi}(l_{TF}) - F_{SX}^{\Delta\Psi}(0) \,. \tag{4}$$

Combined with the previous equation, this leads to

$$\frac{\Delta F_{SX}^{\Delta\Psi}(l_{TF})}{\mathcal{A}} = \frac{\Delta F_{SX}^{0}(l_{TF})}{\mathcal{A}} + \frac{C_{SX}(0) - C_{SX}(l_{TF})}{2}\Delta\Psi^2 \,, \tag{5}$$

(see the thermodynamic cycle in *SI Appendix*). We now introduce

$$\Delta\Delta F_{SX}^{\Delta\Psi}(l_{TF}) = \Delta F_{SX}^{\Delta\Psi}(l_{TF}) - \Delta F_{SV}^{0}(l_{TF}) \,, \tag{6}$$

which can be efficiently obtained from simulations using the method presented below. Noting that for $\Delta\Psi = 0$ V, the two interfaces of each capacitor are identical, this quantity provides the link with the difference in interfacial tensions and contact angle (see Eq. 2)

$$\Delta\Delta F^0_{SL}(l_{TF}) = -2\mathcal{A}\gamma_{LV}\Delta\cos\theta(l_{TF})\ . \tag{7}$$

The computation of free energies using molecular simulations requires dedicated approaches, typically involving a thermodynamic path from a reference state with known properties. One possibility is to compute the work of adhesion of the liquid on each surface, as done in Ref. 50 to compare two models of gold in contact with an ionic liquid, in the absence of voltage. Here, we introduce instead a thermodynamic integration approach, to efficiently compute the free energy change, for a given capacitor and fixed voltage, as a function of the Thomas-Fermi length l_{TF}.

Thomas-Fermi Thermodynamic Integration

The classical description of metallic electrodes at constant potential using fluctuating charges [33, 34] was recently extended to materials characterized by a finite l_{TF} [51]. In a nutshell, the system involves mobile molecules and ions of the electrolyte, with N point charges at positions $\mathbf{r}^N$, and M immobile electrode atoms with atom-centered Gaussian charge distributions with fluctuating magnitudes $\mathbf{q}$ representing the excess charge. The potential energy $\mathcal{U}_{TF}$ entering in the model Hamiltonian of the system (see *SI Appendix*) can be written as

$$\mathcal{U}_{TF}(\mathbf{r}^N, \mathbf{q}) = \frac{\mathbf{q}^T\mathbf{A}(l_{TF})\mathbf{q}}{2} - \mathbf{q}^T\mathbf{B}(\mathbf{r}^N) + \mathcal{C}(\mathbf{r}^N)\ , \tag{8}$$

with $\mathbf{B}$ the vector containing the electrostatic potentials due to the electrolyte on each electrode atom, $\mathcal{C}$ a scalar consisting of all the terms not depending on the electrode charges $\mathbf{q}$, and the matrix

$$\mathbf{A}(l_{TF}) = \mathbf{A}_0 + \frac{l_{TF}^2 d}{\epsilon_0}\mathbf{I}\,. \tag{9}$$

$\mathbf{A}_0$ is the electrostatic interaction matrix between electrode atoms for $l_{TF} = 0$, which depends on their positions and the width of the Gaussian distributions and takes into account the periodicity of the system imposed in molecular simulations of condensed matter [34, 47, 53], d is the atomic density of the electrode, ϵ_0 the vacuum permittivity and $\mathbf{I}$ is the identity matrix.

In practice, the set of electrode charges is determined at each time step in order to satisfy the constant potential and the electroneutrality constraints. Such Born-Oppenheimer (BO) dynamics suppress some charge fluctuations from the original constant-potential ensemble, and their effect must be taken into account separately when evaluating some properties such as the differential capacitance [36]. This is also true for the free energy, obtained from the partition function for a system at fixed $NVT\Delta\Psi$ as $F(l_{TF}) = -k_BT\ln\mathcal{Z}(l_{TF})$. We show in *SI Appendix*, using thermodynamic integration between the perfect metal case ($l_{TF} = 0$) and a non-perfect metal with finite l_{TF} and extending the statistical mechanics derivations of Ref. 36 to non-ideal metals, that the free energy difference defined in Eq. 4 is given by

$$\Delta F^{\Delta\Psi}_{SX}(l_{TF}) = \Delta F^{nBO}(l_{TF}) + \int_0^{l_{TF}} \mathrm{d}l\, \frac{ld}{\epsilon_0}\left\langle (\mathbf{q}^*)^T\mathbf{q}^*\right\rangle_{l,\Delta\Psi}\ , \tag{10}$$

where $\Delta F^{nBO}(l_{TF})$ is the contribution beyond BO sampling, $\mathbf{q}^* = \{q_1, \ldots, q_M\}$ are the instantaneous electrode charges in the BO dynamics (for simplicity, we drop the exponent when referring to individual charges), and the ensemble average of the sum of their squares is taken at fixed screening length l and voltage $\Delta\Psi$. Even though the integrand can be expressed simply with the charges, its origin is the kinetic energy of the electron (treated at the Thomas-Fermi level), as discussed in *SI Appendix*, and the ensemble average ensures that the effect of all electrostatic and non-electrostatic interactions is taken into account, since they all contribute to the relative weights of microscopic configurations explored by the system.

For the empty capacitor with $\Delta\Psi = 0$ V, there is no BO contribution because no charges are induced on the surface. It then follows from Eq. 10 that $\Delta F^{nBO}(l_{TF}) = \Delta F^0_{SV}(l_{TF})$ only depends on the electrode configuration, *i.e.* neither on the presence or absence of electrolyte nor on voltage, and therefore cancels out in differences. In particular, the difference introduced in Eq. 6 reduces to the BO contribution to the free energy difference sampled by molecular

dynamics:

$$\frac{\Delta\Delta F_{SX}^{\Delta\Psi}(l_{TF})}{\mathcal{A}} = \int_0^{l_{TF}} \mathrm{d}l \, \frac{ld}{\epsilon_0 \mathcal{A}} \left\langle (\mathbf{q}^*)^T \mathbf{q}^* \right\rangle_{l,\Delta\Psi} . \tag{11}$$

Eq. 11 provides the practical expression to apply our thermodynamic integration approach as a function of the metallicity of the electrode. It only requires a set of independent simulations for an ensemble of l_{TF} values, during which the integrand is straightforwardly obtained from the atomic electrode charges, thereby bypassing the expensive computation of free energies for each l_{TF}.

Empty capacitor

We first consider the case of an empty capacitor, consisting of two graphite electrodes of surface area $\mathcal{A}$, each with $n = 50$ layers with interplane distance a, separated by a range of distances L between the first atomic planes (see Fig. 2a), held at a potential difference $\Delta\Psi = 1$ V. In such a system, the total charge on each electrode is well predicted by continuum theories, the charge per plane decreases exponentially within the electrode (with a decay length l_{TF}) and is homogeneous within each atomic plane [51]. By further assuming that the number of planes is large, one can write the charge per plane (indexed by $k \in [\![1, \infty[\![$ in each electrode) as $Q_k = \pm Q e^{-(k-1)a/l_{TF}}(1 - e^{-a/l_{TF}})$. Introducing m the number of atoms per plane, related to the atomic density of the electrode by $d = m/a\mathcal{A}$, and the capacitance $C_{SV}(l_{TF}) = \epsilon_0/(L + 2l_{TF})$ corresponding to a vacuum slab and two Thomas-Fermi electrodes in series, Eq. 11 finally leads to

$$\frac{\Delta\Delta F_{SV}^{\Delta\Psi}(l_{TF})}{\mathcal{A}} = 2\epsilon_0 \Delta\Psi^2 \int_0^{l_{TF}} \mathrm{d}l \, \frac{1}{(L+2l)^2} f\left(\frac{a}{l}\right) , \tag{12}$$

where $f(x) = \frac{1}{x}\sum_{k=1}^{\infty} e^{-2(k-1)x}(1 - e^{-x})^2 = \frac{(1-e^{-x})^2}{x(1-e^{-2x})}$ comes from summing over the electrode planes. In the continuum limit ($a \to 0$), this expression simplifies to $\Delta\Delta F_{SV}^{\Delta\Psi}(l_{TF}) \approx \epsilon_0 \mathcal{A} l_{TF} \Delta\Psi^2 / L(L + 2l_{TF})$, consistently with Eqs. 5-6. For insulating materials ($l_{TF} \to \infty$), the difference with respect to perfect conductors further reduces to $\Delta\Delta F_{SV}^{\Delta\Psi}(\infty) \approx \epsilon_0 \mathcal{A} \Delta\Psi^2 / 2L$.

Results from the calculations with explicit electrode atoms are given in Fig. 2b-c for the average $\left\langle (\mathbf{q}^*)^T \mathbf{q}^* \right\rangle / \mathcal{A}$ and the free energy difference per unit area as a function of the Thomas-Fermi length. The evolution of $\Delta\Delta F_{SV}^{\Delta\Psi}(l_{TF})$ as a function of both l_{TF} and L is very well described by Eq. 12. We have also checked the quadratic dependence of the result with the voltage $\Delta\Psi$ (values for $\Delta\Psi = 2$ V are given in Fig. S1 in *SI Appendix*). We finally note that in the absence of an electrolyte, for this typical voltage of 1 V the order of magnitude of the change in free energy per unit area due to a change in metallicity is small compared *e.g.* to the liquid-vapor surface tension of water γ_{LV} or even to $\Delta\gamma_{SL}(\infty) - \Delta\gamma_{SV}(\infty)$ deduced from the contact angles (see Eq. 2).

Electrochemical cell

We now move to the more complex case of an electrochemical cell consisting of the same graphite electrodes (with only $n = 5$ planes, which reduces the accessible range of l_{TF} values) separated by a distance L, with a 1M NaCl aqueous solution as electrolyte, in the absence of voltage ($\Delta\Psi = 0$ V). In contrast to conventional dielectric capacitors, there is no electric field in the system beyond the interfacial regions even under applied voltage, due to the screening of the field by the electric double layers (see Fig. S2 in *SI Appendix*). This system is shown in Fig. 2d, while the results for the evolution of $\left\langle (\mathbf{q}^*)^T \mathbf{q}^* \right\rangle / \mathcal{A}$ and of $\Delta\Delta F_{SL}^{0V}/\mathcal{A}$ as a function of l_{TF} are shown in panels 2e-f. $\Delta\Delta F_{SL}^{0V}$ increases with l_{TF}, with a shape similar to but different from $\Delta\Delta F_{SV}^{1V}$, and is more than an order of magnitude larger than the latter. The solid line in panel 2f corresponds to an empirical fit of the form (see also Eq. 18 below)

$$\frac{\Delta\Delta F_{SL}^{0V}(l_{TF})}{\mathcal{A}} = 2k_B T \int_0^{l_{TF}} \mathrm{d}l \, \frac{1}{\gamma_0 + \gamma_2 l^2} f\left(\frac{a}{l}\right) , \tag{13}$$

with f defined below Eq. 12, and where γ_0 and γ_2 are two parameters adjusted on $\left\langle (\mathbf{q}^*)^T \mathbf{q}^* \right\rangle / \mathcal{A}$ (panel 2e). At this stage, we will only emphasize that its extrapolation for $l_{TF} \to \infty$ is consistent with the value obtained from the

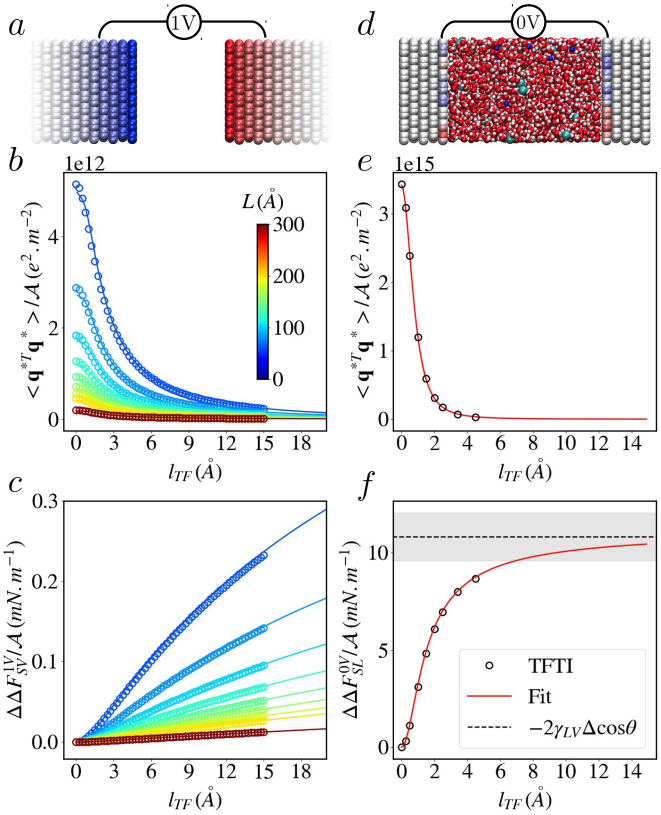

FIG. 2: Thomas-Fermi Thermodynamic Integration (TFTI). (a) Empty capacitor consisting of two graphite electrodes at $\Delta\Psi = 1$ V, separated by a variable distance L ranging from 60.0 to 300.0 Å corresponding to different colors in panels b and c. (b) Average sum of the square of the atomic electrode charges, per unit area, as a function of l_{TF}. (c) Free energy difference per unit area $\Delta\Delta F^{1V}_{SV}(l_{TF})/\mathcal{A}$ due to a change in the Thomas-Fermi length (see Eq. 6), as a function of l_{TF}, computed from Eq. 11. (d) Capacitor consisting of two graphite electrodes at $\Delta\Psi = 0$ V, separated by a distance $L = 56.2$ Å, and a 1M NaCl aqueous solution. (e) Same as panel b for the aqueous capacitor. (f) Free energy difference per unit area $\Delta\Delta F^{0V}_{SL}(l_{TF})/\mathcal{A}$ and asymptotic prediction from contact angles using Eq. 7 (for the difference between metallic and insulator, with $l_{TF} = 0$ and $l_{TF} \to \infty$, respectively). In panels b-c and e-f, open circles are simulation data, while solid lines are the analytical expression Eq. 12 for panel c (and corresponding for b) and a fit of the form Eq. 13 for panel f (and corresponding for e), with parameters adjusted on the simulation data of panel e.

difference in contact angles, also indicated as a dashed line in panel 2f. This further validates our thermodynamic integration approach to compute free energy differences as a function of l_{TF}. In addition, the transition from metallic to insulating behavior occurs mainly for l_{TF} in the range of a few Å. To illustrate the general applicability of this method on a different system, we also investigated a model electrochemical cell consisting of two gold electrodes with their (100) face in contact with a 1M NaCl aqueous solution (see snapshot in Fig. 3). The comparison with the graphitic system, provided in Fig. S3 of *SI Appendix*, shows a similar trend and a difference in magnitude mainly due to the lower atomic density of gold, highlighting the impact of the geometry on the interfacial free energy difference.

Effect of voltage on interfacial free energies

Fig. 3 illustrates the effect of voltage $\Delta\Psi$ on the interfacial free energy, for the previous gold/1 M NaCl cell. The free energy difference $\Delta F^{\Delta\Psi}_{SL}(l_{TF})$ with respect to the case of a perfect conductor (see Eq. 4) follows the expected quadratic dependence on voltage and is in perfect agreement with the prediction Eq. 5, using the capacitances $C(0)$ and $C(l_{TF})$ obtained from the average charge of the electrodes (the same capacitance is obtained at 1 and 2 V).

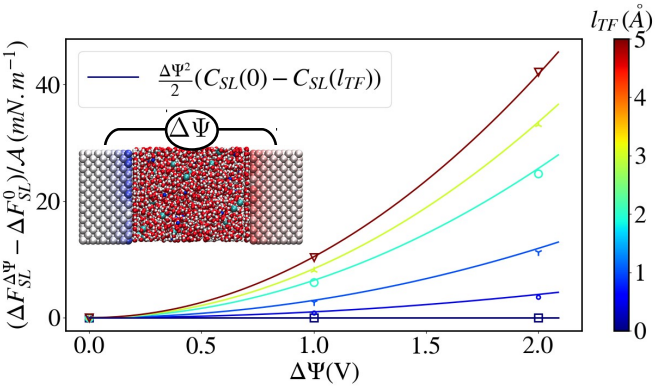

FIG. 3: Effect of voltage $\Delta\Psi$. Free energy change $\Delta F_{SL}^{\Delta\Psi}(l_{TF})$ with respect to the case of a perfect conductor (see Eq. 4) as a function of $\Delta\Psi$ in the case of an electrochemical cell consisting of a 1M NaCl aqueous electrolyte between gold electrodes (see inset). Results are shown per unit area, after subtraction of the value in the absence of voltage, $\Delta F_{SL}^{0}(l_{TF})$. The simulation results (symbols) are shown for several values of the Thomas-Fermi length l_{TF}, indicated by their color, and compared to the quadratic prediction Eq. 5 (lines) using the capacitances per unit area determined from the average charge.

Microscopic origin: the role of lateral correlations

Overall, the above results demonstrate the relevance of molecular simulations combined with our thermodynamic integration as a function of l_{TF} in order to investigate the effect of metallicity and voltage on interfacial free energies. Importantly, Eq. 11, derived from statistical-physical considerations, emphasizes the role of the atomic charge distribution within the metal. In the following, we further exploit the possibilities offered by molecular simulations to investigate the microscopic origin of this charge distribution and the effect of metallicity on the latter.

Metallicity changes lateral charge correlations in the solid

The heterogeneity of the charge distribution within the metal reflects both the structure of the interfacial fluid and how the metal is polarized by each source. While the structure of water in the first adsorbed layer hardly depends on the screening length l_{TF} (see Figs. S4 and S5 in *SI Appendix*), the latter has a large influence on the charge distribution, as illustrated for the first electrode plane in Figs. 4a and 4b, for the previous graphite-aqueous NaCl systems (with a four times larger surface area), at $\Delta\Psi = 0V$. Fig. 4c then shows the corresponding in-plane charge-charge correlation function $g_{qq}(r) = \langle \delta q(r)\delta q(0)\rangle \,/\, \langle \delta q^2 \rangle$, with $\delta q = q - \langle q \rangle$ the local deviation from the average charge in the first electrode plane (see *SI Appendix* for more details). The decay of $g_{qq}(r)$ is slower for larger l_{TF}, consistently with the decay of the charge distribution inside the metal induced by an external point charge [51]. In order to quantify the extent of these lateral correlations, we introduce the correlation surface

$$S_{\text{corr}} = \int_0^\infty g_{qq}(r) 2\pi r \mathrm{d}r \;, \tag{14}$$

which will be discussed below. Similar quantities can be defined for each electrode plane k. For a homogeneous charge distribution (as in empty capacitors), $S_{\text{corr}} \to \infty$, while for a completely random charge distribution, $S_{\text{corr}} = S_1 = \mathcal{A}/m$, the area per atom. In practice, for a perfect metal ($l_{TF} = 0$), the correlation length corresponding to S_{corr} reflects that of the interfacial fluid [35]. Fig. 4d shows the running integral corresponding to Eq. 14. Even though the finite box size does not allow to reach a plateau for large r, the inset shows that the value of the running integral at half the box size is roughly independent of the latter and the corresponding value will be used in the discussion below.

From charge correlations to interfacial free energies

We now use the above microscopic information on the charge distribution to derive a simple model of the surface free energy to understand its evolution with l_{TF} and with voltage. Starting from Eq. 11, we group the sum of the

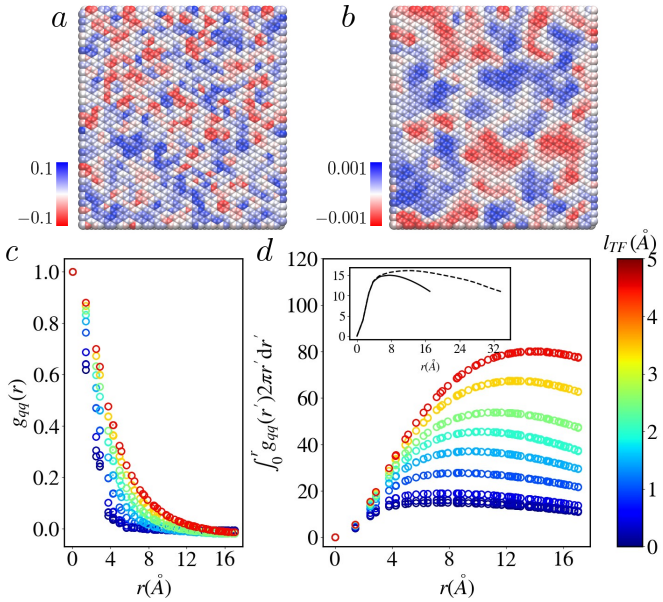

FIG. 4: Effect of metallicity on lateral charge correlations. Instantaneous charge distribution (color bar in units of the elementary charge e) on the first electrode plane for $l_{TF} = 0.0$ Å (a) and $l_{TF} = 4.5$ Å (b), for a 1M NaCl / graphite capacitor at $\Delta\Psi = 0$ V. Charge-charge radial distribution function $g_{qq}(r)$ in the first atomic plane (c) and its integral $\int_0^r g_{qq}(r')2\pi r'\mathrm{d}r'$ (d) for a range of l_{TF} values. The inset of panel (d) shows the integral of g_{qq} for $l_{TF} = 0.0$ for the main simulation box (solid line) and for one with double size in the x and y directions (dashed line, corresponding to the snapshots a and b).

square of atomic charges $\left\langle (\mathbf{q}^*)^T\mathbf{q}^*\right\rangle$ by planes and express, within each plane k, the contribution of each atom to the sum as $\left\langle q_k^2\right\rangle = \left\langle q_k\right\rangle^2 + \left\langle \delta q_k^2\right\rangle$. The first term is simply $\left\langle Q_k\right\rangle^2/m^2$, with the average charge of the plane and the number of atoms per plane. For the second, we introduce $\alpha_k = m\left\langle \delta q_k^2\right\rangle / \left\langle \delta Q_k^2\right\rangle$ to relate the atomic charge fluctuations to that of the plane. We then consider the charge $Q_\mathcal{S} = \frac{m}{\mathcal{A}}\iint_\mathcal{S} \mathrm{d}\mathcal{S}\,\delta q(\mathbf{r})$ of a surface element $\mathcal{S}$ much larger than the correlation length and approximate (see Ref. 35)

$$\begin{aligned}\left\langle (\delta Q_\mathcal{S})^2\right\rangle &= \left(\frac{m}{\mathcal{A}}\right)^2 \iint_\mathcal{S} \mathrm{d}\mathcal{S}' \iint_\mathcal{S} \mathrm{d}\mathcal{S}\ \left\langle \delta q(\mathbf{r})\delta q(\mathbf{r}')\right\rangle \\ &\approx \left(\frac{m}{\mathcal{A}}\right)^2 \mathcal{S}\left\langle \delta q^2\right\rangle \int_0^\infty g_{qq}(r)2\pi r\mathrm{d}r\ ,\end{aligned} \tag{15}$$

by introducing the relative position r in polar coordinates and extending the integral to infinity. Applying this relation to a whole electrode plane with area $\mathcal{A}$ and introducing the correlation surface Eq. 14, we obtain $\alpha_k = S_1/S_{\mathrm{corr,k}}$. Summing over the m atoms in each plane, and over the planes of both electrodes leads to $\left\langle (\mathbf{q}^*)^T\mathbf{q}^*\right\rangle \approx 2\sum_{k=1}^{\infty}\left[\frac{\langle Q_k\rangle^2}{m} + \frac{\left\langle \delta Q_k^2\right\rangle S_1}{S_{\mathrm{corr},k}}\right]$. We then make two assumptions, discussed below, (i) that the charge decays exponentially within the electrode, to relate the charge of each plane to the total charge Q of the electrode, and (ii) that the correlation surface is the same in all planes. Performing the sums over planes as for the empty capacitor, we obtain

$$\frac{\left\langle (\mathbf{q}^*)^T\mathbf{q}^*\right\rangle}{\mathcal{A}} \approx \frac{2S_1 a}{l_{TF}} f\left(\frac{a}{l_{TF}}\right)\left[(C_{\mathrm{int}}\Delta\Psi)^2 + \frac{k_B T C_{\mathrm{diff}}^{BO}}{S_{\mathrm{corr}}}\right] \tag{16}$$

using the function f defined below Eq. 12 and that the total charge can be expressed using the integral capacitance per unit area $Q = C_{\mathrm{int}}\mathcal{A}\Delta\Psi$, while its fluctuations provide the electrolyte (Born-Oppenheimer) contribution to the differential capacitance per unit area [36] as $C_{\mathrm{diff}}^{BO} = \left\langle \delta Q^2\right\rangle/(k_B T\mathcal{A})$. Introducing the above results in Eq. 11 finally yields

$$\Delta\Delta F_{SL}^{\Delta\Psi}(l_{TF}) = \Delta\Delta F_{SL}^{0V}(l_{TF}) + \mathcal{B}\Delta\Psi^2 \tag{17}$$

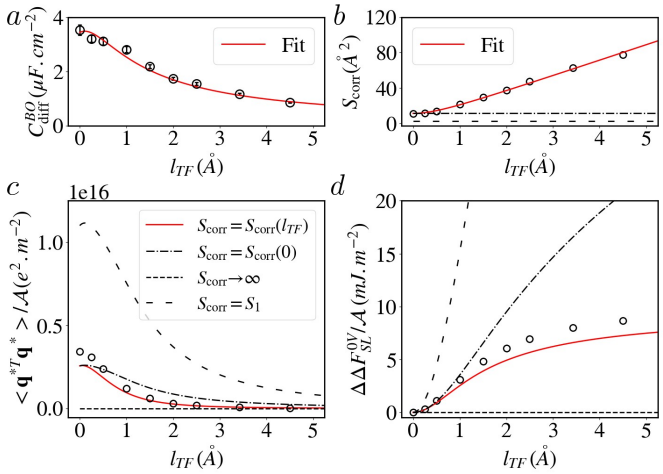

FIG. 5: From charge correlations to interfacial free energies. (a) Differential capacitance $C_{\rm diff}^{BO}$ as a function of the Thomas-Fermi length l_{TF} computed from the electrode charge fluctuations at $\Delta\Psi = 0.0$ V, for a 1M NaCl / graphite capacitor (open black circles); the line is a fit (see section *From Charge Correlations to Interfacial Free Energies*) used in panels (c) and (d). (b) Correlation surface $S_{\rm corr}$ obtained from the charge-charge correlation function (see Eq. 14); the solid red line is a fit (see section *From Charge Correlations to Interfacial Free Energies*) used in panels (c) and (d), while the dashed black line indicates the area per atom $S_1 = \mathcal{A}/m$ and the dash-dotted black line the constant value $S_{\rm corr}(l_{TF} = 0)$. Average squared charges per unit area $\langle(\mathbf{q}^*)^T\mathbf{q}^*\rangle/\mathcal{A}$ (c) and interfacial free energy difference per unit area $\Delta\Delta F_{SL}^{0V}(l_{TF})/\mathcal{A}$ (d): simulation results (symbols) are compared to the predictions of Eqs. 16 and 18 (solid red line) using the fits of panels (a) and (b) or neglecting the dependence of $S_{\rm corr}$ with l_{TF}, *i.e.* assuming perfectly metallic ($S_{\rm corr}(l_{TF}) = S_{\rm corr}(0)$, dash-dotted line), homogeneous ($S_{\rm corr} \to \infty$, dotted line) or uncorrelated ($S_{\rm corr} = S_1$, dashed line) charge distributions.

where

$$\frac{\Delta\Delta F_{SL}^{0V}(l_{TF})}{\mathcal{A}} = \frac{2k_BT}{\epsilon_0}\int_0^{l_{TF}} \mathrm{d}l\, \frac{C_{\rm diff}^{BO}(l)}{S_{\rm corr}(l)} f\left(\frac{a}{l}\right), \tag{18}$$

and $\mathcal{B} = \frac{2\mathcal{A}}{\epsilon_0}\int_0^{l_{TF}} \mathrm{d}l\, C_{\rm int}(l)^2 f\left(\frac{a}{l}\right) \xrightarrow[a\to 0]{} \frac{\mathcal{A}}{\epsilon_0}\int_0^{l_{TF}} \mathrm{d}l\, C_{\rm int}(l)^2$. In the continuum limit ($a \to 0$), we find that Eq. 17 reduces to Eqs. 4, 5 and 6 when $1/C_{\rm int}(l_{TF}) = 1/C_{\rm int}(0) + 2l_{TF}/\epsilon_0$, which corresponds to an ideal capacitor in series with two Thomas-Fermi electrodes.

Beyond the potential-dependent part, the present analysis highlights the deep connection between the interfacial free energy and the charge correlations within the metal, as evident from the presence of the correlation surface $S_{\rm corr}$ in Eq. 18. This simple model only requires the evolution of the differential capacitance $C_{\rm diff}^{BO}$ and $S_{\rm corr}$ with l_{TF} to compute $\Delta\Delta F_{SL}^{0V}(l_{TF})/\mathcal{A}$. Results from simulations at $\Delta\Psi = 0$ V are shown in Figs. 5a and 5b, respectively, together with empirical fits of the form $C_{\rm diff}^{BO} = \epsilon_0/(\gamma_0' + 2l_{TF} + \gamma_1'/(\gamma_2' + l_{TF}))$ and $S_{\rm corr} = \sqrt{\gamma_0'' + \gamma_2'' l_{TF}^2}$ for further use. When the Thomas-Fermi length increases, the capacitance decreases due the delocalization of the charge deeper inside the surface which screens the potential (consistently with the equivalent circuit picture of capacitors in series, often introducing a so-called "quantum capacitance" to describe the properties of the metal [18, 54]); this delocalization also manifests laterally with an increase in the correlation area.

Fig. 5c then compares $\left\langle(\mathbf{q}^*)^T\mathbf{q}^*\right\rangle/\mathcal{A}$ measured in simulations to the approximation Eq. 16 using the above-mentioned fits of $C_{\rm diff}^{BO}$ and $S_{\rm corr}$. Also shown are the predictions of this approximation when neglecting the dependence of $S_{\rm corr}$ with l_{TF}, *i.e.* assuming perfectly metallic ($S_{\rm corr}(l_{TF}) = S_{\rm corr}(0)$), homogeneous ($S_{\rm corr} \to \infty$) or uncorrelated ($S_{\rm corr} = S_1$, the surface per atom) charge distributions. Even though some deviations are observed for small l_{TF}, the agreement is remarkable when considering $S_{\rm corr}(l_{TF})$, unlike either of the two extreme distributions. Fig. 5d finally shows the same comparison for $\Delta\Delta F_{SL}^{0V}(l_{TF})$, now with Eq. 18. The deviations are now more evident for large l_{TF}, due to the accumulation of errors upon integration, but the semi-quantitative agreement obtained when considering $S_{\rm corr}(l_{TF})$, compared to the dramatic failure of both the random and homogeneous distributions and even assuming that the correlations are the same as in the perfect metal case, confirms the crucial role of charge correlations within the metal on the evolution of the interfacial free energy with l_{TF}.

As noted above, the transition from metallic to insulating behavior of the interfacial free energies occurs mainly for l_{TF} in the range of a few Å. Translating the correlation area into an effective correlation length $l_{\rm corr}(l_{TF}) = \sqrt{S_{\rm corr}(l_{TF})/\pi}$ (which corresponds to approximating $g_{qq}(r)$ by a Heaviside function), we find that this range corresponds to a change from $l_{\rm corr} \approx 1.9$ Å for $l_{TF} = 0$ to $l_{\rm corr} \approx 5.0$ Å for $l_{TF} = 4.5$ Å. We can compare this to the position of the first maximum of the two-dimensional (2D) radial distribution function of water molecules in contact with the surface, $r_{OO}^{2D} \approx 2.7$ Å (see Fig. S4 in *SI Appendix*). This supports the conclusion that the transition for the free energy corresponds to a change from a regime where the charge correlations reflect the structure of the liquid to another where the poor screening within the metal gradually homogenizes the charge distribution.

Discussion

In order to explain the remaining difference between the exact result Eq. 11 and the approximation Eq. 18, we examine the assumptions that allowed us to obtain this simple expression. Beyond the convergence of the integral defining $S_{\rm corr}$ (Eq. 14) for a finite-size system, discussed above, the convergence of the estimate of the integrand in Eq. 11 (reached within a few ns, see Fig. S6 in *SI Appendix*) and the possible errors due to the numerical integration in Eq. 11 that can be reduced systematically by increasing the number of simulated l_{TF} values, we have assumed that the charge decays exponentially within the electrode, with a decay length l_{TF}. Such an assumption is consistent, for the average charge in each plane, with the observation that for a finite voltage the average potential decays exponentially within the electrodes (as shown for gold electrodes in Ref. 51). For the charge fluctuations also considered in the present model, we test it for $\Delta\Psi = 0V$ by considering $\langle \delta Q_k^2 \rangle / \langle \delta Q^2 \rangle$, reported for a range of l_{TF} values and a 1M NaCl / graphite capacitor in Fig. 6a. The exponential assumption is satisfied, except for very small l_{TF} (smaller than the interplane distance a), and the corresponding decay length is $l_{TF}/2$, as expected.

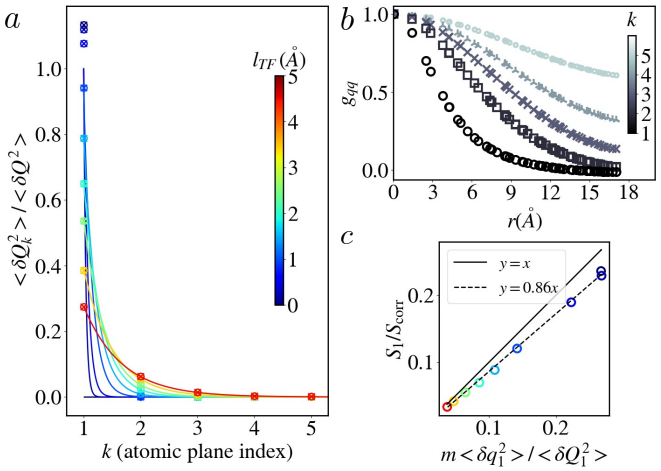

FIG. 6: Testing the assumptions of the model for a 1M NaCl / graphite capacitor at $\Delta\Psi = 0.0$ V. (a) Ratio between the variance of the charge of each plane k and that of the total charge of the electrode, $\langle \delta Q_k^2 \rangle / \langle \delta Q^2 \rangle$, for a range of l_{TF} values from 0.0 to 4.5 Å indicated by the colorbar; the lines are analytical predictions for an exponential decay, with a the interplane distance and a decay length $l_{TF}/2$. (b) In-plane charge-charge radial distribution function g_{qq} as a function of the distance r for $l_{TF} = 4.5$ Å for the different planes of the electrodes, where k is the atomic plane index from 1, in contact with the electrolyte (black circles) to 5 (light grey small circles). (c) Ratio $S_1/S_{\rm corr}$ as a function of $m \langle \delta q_1^2 \rangle / \langle \delta Q_1^2 \rangle$ in the first atomic plane, for a range of l_{TF} shown in the colorbar. The solid black line corresponds to $y = x$ while the dashed line is a fit of the form $y = \gamma x$.

We further assumed that the correlation surface $S_{\rm corr,k}$ is the same in all electrode planes and used the value $S_{\rm corr}$ measured in the first plane in contact with the liquid. Fig. 6b shows the charge-charge correlation function in the five planes for $l_{TF} = 4.5$ Å and clearly demonstrates that this assumption is not accurate. Its shortcomings are however mitigated by the exponential decay of the contribution of each plane. Finally, we introduced the correlation surface to link the atomic charge fluctuations to those of each plane, which required assuming in particular that the area of the electrode, $\mathcal{A} \approx 1250$ Å^2, is much larger than $S_{\rm corr}$: Fig. 5b confirms that this is indeed the case. The ratio $m \langle \delta q_1^2 \rangle / \langle \delta Q_1^2 \rangle$ can also be estimated directly and is compared to $S_1/S_{\rm corr}$ in Fig. 6c. While the agreement is not quantitative, the linear correlation with a slope ≈ 1.2 clearly supports our microscopic interpretation of the effect of

metallicity on the interfacial free energy, via the lateral charge correlations within the metal. We further note that the Thomas-Fermi screening length also influences the dynamics of the charge induced in the metal (see Fig. S6 in *SI Appendix*), but interpreting these changes in terms of the effect of metallicity on the dynamics of the interfacial electrolyte remains an open challenge requiring further investigation.

Even though a comprehensive molecular simulation study of the crystallisation of ionic liquids remains out of the scope of this work, we finally examine the implications of our semi-analytical model, Eq. 18, whose assumptions do not depend on the nature of the electrolyte considered in the present work, for the interpretation of the experiments of Ref. 12. The link between interfacial free energies and the shift in the melting/crystallization temperature induced by the interactions with the walls is provided by the Gibbs-Thomson equation [55, 56], which involves the difference in surface tension $\Delta\gamma = \gamma_{LW} - \gamma_{SW}$ between the liquid and the walls and between the solid and the walls, respectively. For a given electrode, we anticipate that the capacitance of the cell is smaller for the solid phase, which behaves as a dielectric material, than for the liquid phase, which can rearrange to form electric double layers. While it will be more challenging to determine numerically in molecular simulations, we also expect a larger correlation surface for the solid than for the liquid. Both effects concur to indicate, according to Eq. 18, that the free energy penalty due to a finite l_{TF} is smaller for the solid ionic phase compared to the liquid one. The above argument suggests that, all other things being equal, increasing l_{TF} should decrease the length at which freezing is observed – in contrast to experimental observations. In experiments, many features beyond l_{TF} change when considering different surfaces (from mica to Pt via graphite and doped Si) and the ability to change the screening length independently of other material properties offers an opportunity to disentangle the various effects, within the Thomas-Fermi model. The above conclusion based on our semi-analytical model remains to be confirmed by future MD simulations, but we note that it is consistent with more recent experiments suggesting that the change in mechanical properties may be associated with a glassy behavior rather than proper phase transition [13].

Conclusion

A thermodynamic integration method as a function of the Thomas-Fermi length allowed us to investigate the effect of the metallic character of solid substrates on interfacial free energies using molecular simulations. This approach was validated against analytical results for empty capacitors and by comparing the predictions in the presence of an electrolyte with values determined from the contact angle of droplets on the surface. The general expression derived in this work highlights the role of the charge distribution within the metal. We proposed a simple semi-analytical model to interpret the evolution of the interfacial free energy with voltage and Thomas-Fermi length, which allowed us to identify the charge correlations within the metal as the microscopic origin of the evolution of the interfacial free energy with the metallic character of the substrate.

This methodology offers avenues for the molecular-scale study of the effect of the metallic character of the substrate on confinement-induced transitions in ionic systems, as reported in AFM and SFA experiments, with the possibility to investigate the relative stability of interfacial crystals with respect to their melt. A quantitative comparison with experiments might require a more refined description of the interface, *e.g.* to capture differences between good metals such as Au and Pt due to non-electrostatic effects that play a role on the interfacial structure, hence on the polarization of the metal [32], or the presence of adsorbed ions [57]. Such features may be better described using *ab initio* MD simulations [58] or hydrid quantum mechanics/molecular mechanics and multiscale approaches to compute solvation free energies [59] or to investigate wetting [60] and the link between surface thermodynamics and slippage [61], even though recent studies suggest that reparameterizing classical models can already provide a step in this direction [62, 63]. Nevertheless, the possibility to systematically assess the effect of the screening length allows to go beyond the analytical calculations for a 1D ionic crystal near a substrate [25] to the full three-dimensional interface, both in solid and liquid phases, and to analyze the effect of lateral correlations. Since the charge distribution is known to have a large impact on solid-liquid friction [64], one could also consider the possibility to extend the present approach to examine the effect of metallicity on dynamical properties. More generally, the present work contributes from a molecular perspective to a broader endeavor to understand interfaces between solvent-based electrolytes and ionic liquids with good metals or carbon surfaces, which are already exploited *e.g.* for energy storage in supercapacitors [65], energy conversion via metal nanolayers [66], or blue energy harvesting and desalination applications [67, 68].

Materials and methods

We perform molecular dynamics simulations of capacitors with two electrodes consisting of atoms bearing a Gaussian charge distribution, separated by vacuum or by an aqueous sodium chloride electrolyte; we also consider droplets of the same electrolyte on a single electrode. The electrode atoms charges are either kept constant and equal to zero

or determined at each time step in order to satisfy a constant potential and an electroneutrality constraints using the conjugate gradient method [36]. The constant potential simulations account for the electronic polarization of the metal and we use an implementation introducing the Thomas-Fermi screening length to tune the metallicity of the metal [51]. All simulations are performed using the MetalWalls code [69] and simulation details, including the description of the systems, the computation of interactions and the constant-potential ensemble are available in the *SI Appendix*. The analysis of the electrode atom charges was performed using in-house Python scripts and provides the capacitance from the total charge of the electrodes, the charge-charge radial distribution functions and corresponding correlation lengths, and the integrand of Eq. 11 resulting in the free energy as a function of the Thomas-Fermi length.

Data availability

MetalWalls [69], the MD code used for this study, is available open-source at `https://gitlab.com/ampere2/metalwalls`. Input files and raw data used for the figures have been deposited in Zenodo [70] (https://doi.org/10.5281/zenodo.5658485).

Acknowledgements

We thank Mathieu Salanne, Lydéric Bocquet, Benoît Coasne and David Limmer for useful discussions. This project was supported by the European Research Council under the European Union's Horizon 2020 research and innovation programme (grant agreement No. 863473). This work was supported by the French National Research Agency (Labex STORE-EX [Laboratory of excellency for electrochemical energy storage], Grant ANR-10-LABX-0076, and project NEPTUNE (From weak to strong non-equilibrium transport of fluids at the nanoscale), Grant ANR-17-CE09-0046-02). We acknowledge high-performance computing resources granted by GENCI (Grand Équipement National de Calcul Intensif) (resources of CINES (Centre Informatique National de l'Enseignement Supérieur), Grant No A0070911054).

Supporting Information

Contact angles

Contact angles were determined from density maps in the (r, z) plane (see Fig. 1c of the main text), with r the radial distance to the center of mass of the droplet and z the height with respect to the first graphite layer. The liquid-vapor interface is located from the points where the average local density is equal to half of the bulk density ρ_0 at the center of the droplet (in blue on Fig. 1c of the main text). This set of points is then fitted using a circle of radius R_C and centered in $(r = 0, z = z_C)$ and the value of the contact angle θ is obtained by the intersection of this fit with the interface plane, taken as the position of the first water layer $z_W = 3.12$ Å. This choice has a small influence on the contact angle values, which is within the errorbars and does not modify the conclusions of the study.

For a homogeneous sphere of density ρ_0, radius R_C and centered in $(r = 0, z = z_C)$, cut by a plane in $z = z_0$ (taken empirically at $z_W/2$), the corresponding one-dimensional densities are given by

$$\rho(z) = \rho_0 \pi (R_C^2 - (z - z_C)^2) \tag{19}$$

$$\rho(r) = \rho_0 \left(z_C - z_0 + \sqrt{R_C^2 - r^2} \right) , \tag{20}$$

shown along with the simulation results in Fig. 1d-e of the main text.

Derivation of the Thomas-Fermi Thermodynamic Integration (TFTI) method

We consider a system of N mobile atoms of electrolyte, with positions $\mathbf{r}^N$ and momenta $\mathbf{p}^N$, and M electrode atoms that carry a Gaussian charge distribution with fluctuating magnitude $\mathbf{q} = \{q_1, q_2, \ldots, q_M\}$, in a finite volume V, at a temperature T and a fixed voltage $\Delta\Psi$ between the electrodes. The free energy associated with a change in Thomas-Fermi (TF) screening length l_{TF} is computed starting from the definition of free energy $F^{\Delta\Psi} = -\beta^{-1} \ln \mathcal{Z}$, with $\mathcal{Z}$ the partition function corresponding to the $NVT\Delta\Psi$ ensemble. From Ref. 51, the extended TF Hamiltonian is

$$\mathcal{H}(\mathbf{r}^N, \mathbf{p}^N, \mathbf{q}) = \mathcal{K}(\mathbf{p}^N) + \mathcal{U}_0(\mathbf{r}^N) + \frac{\mathbf{q}^T \mathbf{A}_{TF} \mathbf{q}}{2} - \mathbf{q}^T \mathbf{B} , \tag{21}$$

where $\mathcal{K}$ is the kinetic energy and $\mathcal{U}_0$ contains the electrostatic interactions within the electrolyte, the non-electrostatic terms (typically represented by simple Lennard-Jones potentials to capture short-range repulsion and long-range dispersion interactions) within the electrolyte and with the electrode atoms, and a constant term involving the energy of the Fermi level. Furthermore, $\mathbf{B}$ is the vector of electrostatic potentials due to the electrolyte on each electrode atom and we introduced a modified symmetric matrix

$$\mathbf{A}_{TF} \equiv \mathbf{A}(l_{TF}) = \mathbf{A}_0 + \frac{l_{TF}^2 d}{\epsilon_0} \mathbf{I} , \tag{22}$$

with $\mathbf{A}_0$ the symmetric $M \times M$ matrix describing the electrode-electrode electrostatic interactions for a perfect metal ($l_{TF} = 0$), d is the atomic density, ϵ_0 the vacuum permittivity and $\mathbf{I}$ the $M \times M$ identity matrix. Even though the term involving l_{TF} can be expressed as a function of the charges $\mathbf{q}$ within the extension of constant-potential simulations to the Thomas-Fermi model of Ref. 51, its origin is not electrostatic but the kinetic energy of the electrons. Because the Hamiltonian is quadratic in the charges $\mathbf{q}$, the statistical mechanics framework derived in Ref. 36 remains valid for the extended constant potential TF simulations.

In the present work, we introduce a new thermodynamic integration approach in order to predict the evolution of the free energy as a function of the Thomas-Fermi length, l_{TF}, given by

$$\Delta F^{\Delta\Psi}(l_{TF}) = F^{\Delta\Psi}(l_{TF}) - F^{\Delta\Psi}(0) = \Delta F^{\Delta\Psi, BO}(l_{TF}) + \Delta F^{nBO}(l_{TF}) , \tag{23}$$

where the separation into Born-Oppenheimer (BO) and non-BO contributions is possible thanks to the factorization of the partition function $\mathcal{Z} = K\mathcal{Z}^{BO}$, where K arises from the suppressed charged fluctuations in the BO approximation (see Ref. 36 for the derivation of this result in the case $l_{TF} = 0$). Since the non-BO term depends only on the electrode, *i.e.* neither on the presence or absence of electrolyte nor on voltage, it cancels in all differences considered in the main text. We provide here a derivation of the expression given in the main text for the BO part of the free

energy. We first write the free energy difference, at fixed voltage, between $l_{TF} = 0$ (perfect metal) and a finite l_{TF}, as the integral of its derivative with respect to l_{TF}

$$\Delta F^{\Delta\Psi,BO}(l_{TF}) = F^{\Delta\Psi,BO}(l_{TF}) - F^{\Delta\Psi,BO}(0) = \int_0^{l_{TF}} \mathrm{d}l \left(\frac{\partial F^{\Delta\Psi,BO}}{\partial l}\right)_{NVT\Delta\Psi} . \tag{24}$$

Using the expression of the partition function in the BO ensemble (see Ref. 36), $\mathcal{Z}^{BO}$, the derivative of $F^{\Delta\Psi,BO} = -\beta^{-1}\ln\mathcal{Z}^{BO}$ with respect to l_{TF} reads

$$\left(\frac{\partial F^{\Delta\Psi,BO}}{\partial l_{TF}}\right) = -\beta^{-1}(\mathcal{Z}^{BO})^{-1}\int \mathrm{d}\mathbf{r}^N \;\; e^{-\beta\mathcal{U}_0(\mathbf{r}^N)}\frac{\beta}{2}\left(\frac{\partial(\mathbf{q}^*)^T\mathbf{A}_{TF}\mathbf{q}^*}{\partial l_{TF}}\right)e^{\frac{\beta}{2}(\mathbf{q}^*)^T\mathbf{A}_{TF}\mathbf{q}^*} \quad = -\frac{1}{2}\left\langle\left(\frac{\partial(\mathbf{q}^*)^T\mathbf{A}_{TF}\mathbf{q}^*}{\partial l_{TF}}\right)\right\rangle , \tag{25}$$

where $\mathbf{q}^*$ is the set of charges that enforce both the constant-potential and electroneutrality constraints

$$\mathbf{q}^*(\mathbf{r}^N) = \mathbf{A}_{TF}^{-1}\left[\mathbf{B} + \mathbf{\Psi} - \chi(\mathbf{r}^N)\mathbf{E}\right] , \tag{26}$$

where we used the Lagrange multiplier χ defined in Ref. 36 and $\mathbf{E} = \{1,\ldots,1\}$ is a vector of size M. Noticing that $\mathbf{A}_{TF}$ and $\mathbf{q}^*$ depend on l_{TF} explicitly but that $\mathbf{B}$ and $\mathbf{\Psi}$ don't, and using standard rules for derivation and matrix algebra, we then write

$$\begin{aligned}
\frac{\partial}{\partial l_{TF}}\left[(\mathbf{q}^*)^T\mathbf{A}_{TF}\mathbf{q}^*\right] &= \frac{\partial}{\partial l_{TF}}\left[(\mathbf{q}^*)^T\mathbf{A}_{TF}\mathbf{A}_{TF}^{-1}\mathbf{A}_{TF}\mathbf{q}^*\right] = \frac{\partial}{\partial l_{TF}}\left[\mathbf{A}_{TF}\mathbf{q}^*\right]^T\mathbf{A}_{TF}^{-1}\left[\mathbf{A}_{TF}\mathbf{q}^*\right] \\
&= \left[\frac{\partial(\mathbf{A}_{TF}\mathbf{q}^*)}{\partial l_{TF}}\right]^T\mathbf{A}_{TF}^{-1}\left[\mathbf{A}_{TF}\mathbf{q}^*\right] + \left[\mathbf{A}_{TF}\mathbf{q}^*\right]^T\left(\frac{\partial\mathbf{A}_{TF}^{-1}}{\partial l_{TF}}\right)\left[\mathbf{A}_{TF}\mathbf{q}^*\right] + \left[\mathbf{A}_{TF}\mathbf{q}^*\right]^T\mathbf{A}_{TF}^{-1}\left[\frac{\partial(\mathbf{A}_{TF}\mathbf{q}^*)}{\partial l_{TF}}\right] \\
&= \left[-\frac{\partial\chi}{\partial l_{TF}}\mathbf{E}\right]^T\mathbf{q}^* + \left[(\mathbf{q}^*)^T\mathbf{A}_{TF}\right]\left(-\mathbf{A}_{TF}^{-1}\frac{\partial\mathbf{A}_{TF}}{\partial l_{TF}}\mathbf{A}_{TF}^{-1}\right)\left[\mathbf{A}_{TF}\mathbf{q}^*\right] + (\mathbf{q}^*)^T\left[-\frac{\partial\chi}{\partial l_{TF}}\mathbf{E}\right] \\
&= 0 + (\mathbf{q}^*)^T\left(-\frac{2l_{TF}d}{\epsilon_0}\mathbf{I}\right)\mathbf{q}^* + 0 = -\frac{2l_{TF}d}{\epsilon_0}(\mathbf{q}^*)^T\mathbf{q}^*
\end{aligned} \tag{27}$$

where we used Eq. 26 from the second to third line and the electroneutrality condition $\mathbf{E}^T\mathbf{q}^* = 0$ from the third to fourth line. Introducing this result in Eqs. 25 and 24, we finally obtain:

$$\Delta F^{\Delta\Psi,BO}(l_{TF}) = F^{\Delta\Psi,BO}(l_{TF}) - F^{\Delta\Psi,BO}(0) = \int_0^{l_{TF}} \mathrm{d}l\,\frac{ld}{\epsilon_0}\left\langle(\mathbf{q}^*)^T\mathbf{q}^*\right\rangle_{NVT\Delta\Psi,l} . \tag{28}$$

We note that this quantity is positive, *i.e.* that the free energy increases from the perfect metal case to one charaterized by a finite l_{TF}. While the expression for the interfacial free energy difference only involves the distribution of the charges, it is not limited to and in fact differs from a purely electrostatic contribution. Indeed, the above derivation shows that the integrand comes from the derivative of a term in the energy which arises from the kinetic energy of the electron. The ensemble average ensures that the effect of all electrostatic and non-electrostatic interactions is taken into account, since they all contribute to the relative weights of microscopic configurations explored by the system.

Thermodynamic cycle

In the main text, we introduce various free energy differences associated with different processes, in particular changing the voltage $\Delta\Psi$ or the Thomas-Fermi length l_{TF}. This is illustrated in the following thermodynamic cycle, changing the screening length vertically and charging or discharging the capacitor horizontally:

$$\begin{array}{ccc}
\{l_{TF}=0,\Delta\Psi=0\} & \xrightarrow{F_{SX}^{\Delta\Psi}(l_{TF}=0)-F_{SX}^{0}(l_{TF}=0)} & \{l_{TF}=0,\Delta\Psi\} \\
-\Delta F_{SX}^{0}(l_{TF})\uparrow & & \downarrow\Delta F_{SX}^{\Delta\Psi}(l_{TF}) \\
\{l_{TF},\Delta\Psi=0\} & \xleftarrow[-F_{SX}^{\Delta\Psi}(l_{TF})+F_{SX}^{0}(l_{TF})]{} & \{l_{TF},\Delta\Psi\}
\end{array}$$

where the subscripts SX can refer to the empty capacitor (SV = solid-vapor) or to the full electrochemical cell (SL = solid-liquid). We also introduce the difference $\Delta\Delta F_{SX}^{\Delta\Psi}(l_{TF}) = \Delta F_{SX}^{\Delta\Psi}(l_{TF}) - \Delta F_{SV}^{0}(l_{TF})$. For the empty capacitor with $\Delta\Psi = 0$ V, $\Delta F_{SV}^{0}(l_{TF})$ has no BO contribution because for zero voltage with no electrolyte, no charges are induced on the surface. It therefore follows that $\Delta F_{SV}^{0}(l_{TF}) = \Delta F^{nBO}(l_{TF})$ for the given set of (fixed) electrodes and, using Eq. 23 above, that $\Delta\Delta F_{SX}^{\Delta\Psi}(l_{TF}) = \Delta F_{SX}^{\Delta\Psi,BO}(l_{TF})$ corresponds to the sole BO contribution to the free energy difference, *i.e.* that obtained directly from the BO sampling in constant-potential simulations (see Eq. 11 of the main text).

Methods

For constant-potential simulations, electrode atoms bear a Gaussian charge distribution of fixed width $\eta^{-1} = 0.56$ Å and magnitude determined at each time step to enforce the constant potential and global electroneutrality constraints using a matrix inversion method (for electrochemical cells) or a conjugate gradient method (for empty capacitors and drop simulations). We consider TF lengths l_{TF} ranging from 0.0 to 15.0 Å for the empty capacitor and from 0.0 to 5.0 Å in the presence of aqueous NaCl electrolyte, to ensure that the depth na of the electrodes, with n the number of atomic planes and a the interplane distance, is larger than l_{TF}. We use two-dimensional boundary conditions (no periodicity in the z direction), with 2D Ewald summation to compute electrostatic interactions in the presence of Gaussian charges [34, 53] and a cutoff of 17.0 Å for both the non-electrostatic interactions, described by truncated shifted Lennard-Jones (LJ) potentials, and the short range part of the Coulomb interactions. Water is modeled by the SPC/E force field [71], while LJ parameters for Na^+ and Cl^- are taken from Ref. 72 and those for carbon and gold electrode atoms are from Refs. 73 and 74, respectively; LJ parameters between different atom types are computed using the the Lorentz-Berthelot mixing rules.

For graphite capacitors, each electrode consists of $n = 50$ (resp. 5) planes for empty capacitors (resp. electrochemical cells) separated by $a = 3.354$ Å, with 480 carbon atoms per plane (surface area $\mathcal{A} = 34.101 \times 36.915$ Å^2); larger simulation boxes were also studied with $\mathcal{A} = 68.202 \times 73.830$ Å^2. The atomic density is therefore $d_{\text{graphite}} = 0.11$ Å^{-3}. Contact angle measurements are made by equilibrating a drop of electrolyte on a single electrode of surface area $\mathcal{A} = 102.302 \times 110.745$ Å^2 (4320 carbon atoms per plane) and only $n = 3$ planes, using constant zero charges or a constant potential condition. The uncertainty reported on the contact angles is the standard error among 5 blocks of the simulations. For gold-like electrodes, the box length in both the x and y directions is $L_x = L_y = 36.630$ Å with 162 atoms per atomic plane, corresponding to an atomic density $d_{\text{gold}} = 0.06$ Å^{-3}. The structure is face-centered cubic with a lattice parameter of 4.07 Å and a (100) surface in contact with the electrolyte. The electrodes consist of $n = 10$ planes, separated by $a = 2.035$ Å and held at a potential difference of $\Delta\Psi = 0, 1$ or 2 V. In all cases, the electrolyte is composed of 2160 water molecules and 39 NaCl ion pairs. The capacitor simulation boxes are equilibrated at atmospheric pressure for 500 ps by applying a constant force to the electrodes (treated as rigid bodies) with $l_{TF} = 0.0$ Å; the electrodes separation is then fixed to the equilibrium value (for which the density in the middle of the liquid slab is equal to its bulk value) $L = 56.2$ Å for graphite electrodes and $L = 50.7$ Å for gold electrodes. For empty graphite capacitors we consider a range of distances from 20.0 to 300.0 Å. Simulations are run with a timestep of 1 fs and the temperature is set at 298 K using a Nosé-Hoover chain thermostat. Capacitor simulations are run for at least 6 ns (those with the larger surfaces for 750 ps), while drop simulations are run for 3 ns. Differential capacitances are computed from the fluctuations of the total charge [35, 36] and errorbars estimated using the standard errors on the variance corrected for data correlations. All simulations are performed using the molecular dynamics code MetalWalls [69].

Water structure in the first adsorbed layer on graphite

Fig. 10 reports the 2D oxygen-oxygen radial distribution function for water molecules in the first layer adsorbed on each electrode, for a range of l_{TF}, in a 1M NaCl / graphite capacitor. The results are identical for all the considered l_{TF} values, with in particular a first maximum for a radial distance ≈ 2.7 Å. Fig. 11 further shows that the orientation of water molecules in the same layers, quantified by the distribution $\cos\theta$, with θ the angle between the molecular dipole and the normal to the electrode surfaces also slightly depends on the Thomas-Fermi screening length.

Lateral charge correlations

The lateral charge correlations are quantified using the in-plane charge-charge radial distribution function $g_k^{qq}(r)$, defined as

$$g_k^{qq}(r) = \frac{\left\langle \delta q_{j,k}^*(r) \delta q_{i,k}^*(0) \right\rangle}{\left\langle \delta q_{i,k}^{*2} \right\rangle} = \frac{\mathcal{A}}{2\pi r m \left\langle \delta q_{i,k}^{*2} \right\rangle} \left\langle \sum_{i=1}^{m} \sum_{j>i} \delta q_{i,k}^* \delta q_{j,k}^* \delta(r_{ij} - r) \right\rangle , \tag{29}$$

where k indicates the plane index, $\mathcal{A}$ is the surface area, m the number of atoms per plane and r_{ij} is the radial distance between electrode atoms i and j belonging to the k^{th} plane. $\left\langle \delta q_{i,k}^{*2} \right\rangle$ is the average individual charge fluctuation in plane k. Here $q_{i,k}$ is the magnitude of the Gaussian charge distribution located at r_i (the 3D shape of the Gaussian distributions is not taken into account), so that g_k^{qq} is a charge-weighted 2D radial distribution function between sites – hence the normalization by $2\pi r m/\mathcal{A}$.

Dynamical properties and convergence of averages

The Thomas-Fermi length l_{TF} also influences dynamical properties. This is illustrated in Fig. 12a, which shows the autocorrelation of the total electrode charge, Q, in the case of a 1M NaCl / graphite capacitor at $\Delta\Psi = 0$ V, for a range of l_{TF}. As already observed on gold electrodes [51], the total charge fluctuations decay faster when l_{TF} increases. While a detailed interpretation of the charge fluctuations in terms of the dynamics of the electrolyte remains a challenging question, such a faster decorrelation reflects the weaker interactions of the electrolyte with the more diffuse charge induced within the electrode.

In the context of the present study of interfacial free energies, it is also of interest to consider the fluctuations of the sum of the squared charges, $(\mathbf{q}^*)^T\mathbf{q}^*$, which appears in the integrand leading to the free energy as a function of l_{TF} (see Eq. 11 of the main text). Its autocorrelation, shown in Fig. 12b, also decays faster with increasing l_{TF}, even though the effect is less pronounced than for the total charge. This last point also explains why the time required to converge the static average $\left\langle (\mathbf{q}^*)^T\mathbf{q}^* \right\rangle$ is comparable for all considered values of l_{TF}: As shown in Fig. 12c, which reports the relative error on this quantity, $\left[\left\langle (\mathbf{q}^*)^T\mathbf{q}^* \right\rangle_t - \left\langle (\mathbf{q}^*)^T\mathbf{q}^* \right\rangle_\infty \right] / \left\langle (\mathbf{q}^*)^T\mathbf{q}^* \right\rangle_\infty$, as a function of the trajectory length t, in all cases the error is already of the order of 1% with a few 10-100 ps and $\left\langle (\mathbf{q}^*)^T\mathbf{q}^* \right\rangle$ is well converged in a few ns.

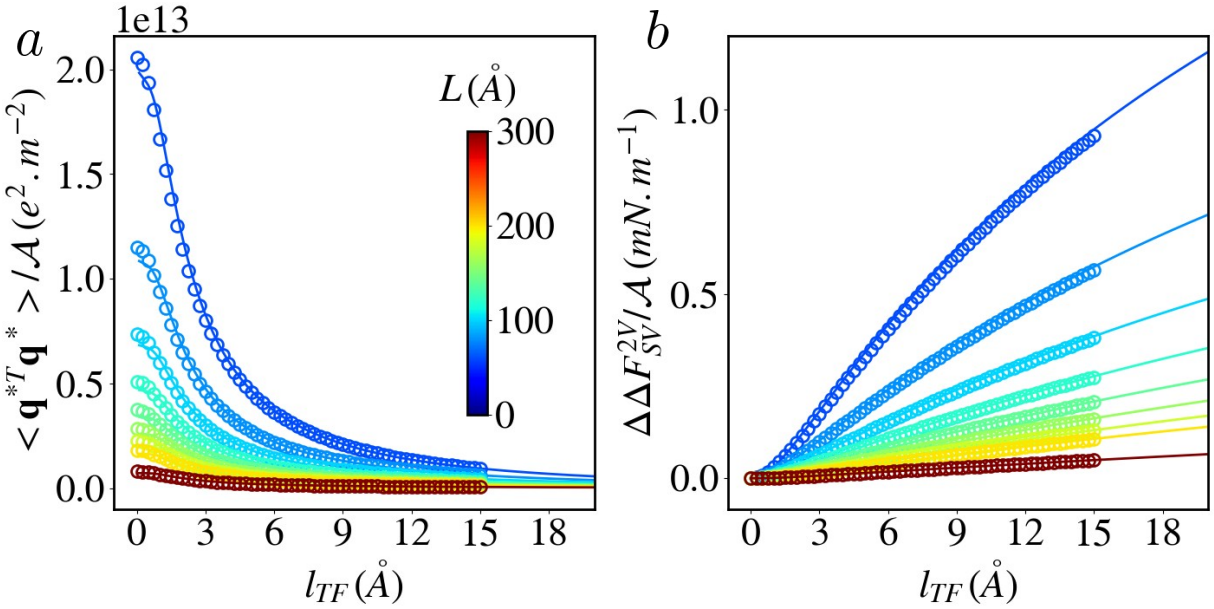

FIG. 7: (a) Average sum of the square of the atomic electrode charges, per unit area, as a function of l_{TF}. (b) Free energy difference per unit area $\Delta\Delta F^{2V}_{SV}(l_{TF})/\mathcal{A}$ due to a change in the Thomas-Fermi length (see Eq. 6 of the main text), as a function of l_{TF}, computed from Eq. 28. Values are shown for an empty capacitor consisting of two graphite electrodes at $\Delta\Psi = 2$ V, separated by a variable distance L ranging from 60.0 to 300.0 Å corresponding to different colors in panels a and b. Open circles are simulation data, while solid lines are the analytical expression Eq. 12 of the main text for panel b and the corresponding one for panel a.

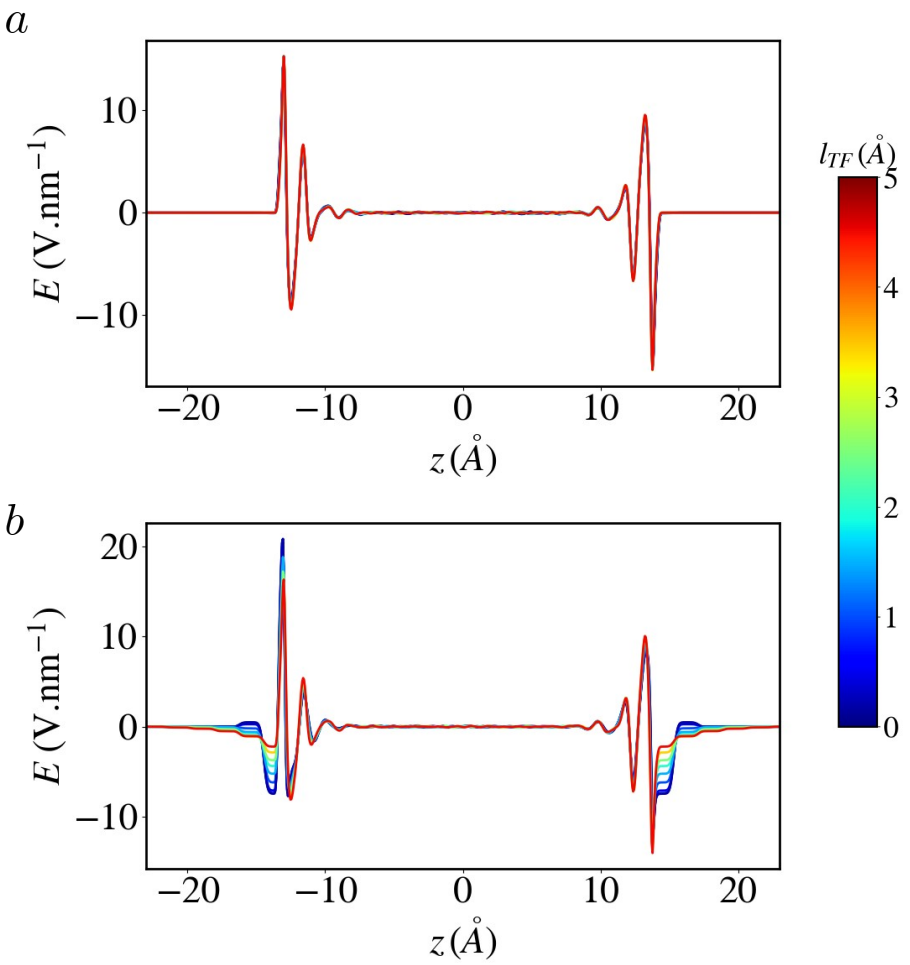

FIG. 8: Electric field profile, computed by integrating the average charge density $\rho_{el}(z)$ with respect to the position z across the cell, for a 1M NaCl / graphite capacitor at $\Delta\Psi = 0$ V (a) and 2 V (b), for a range of l_{TF} indicated by the color bar. There is no average electric field in the bulk region of the capacitor, as expected.

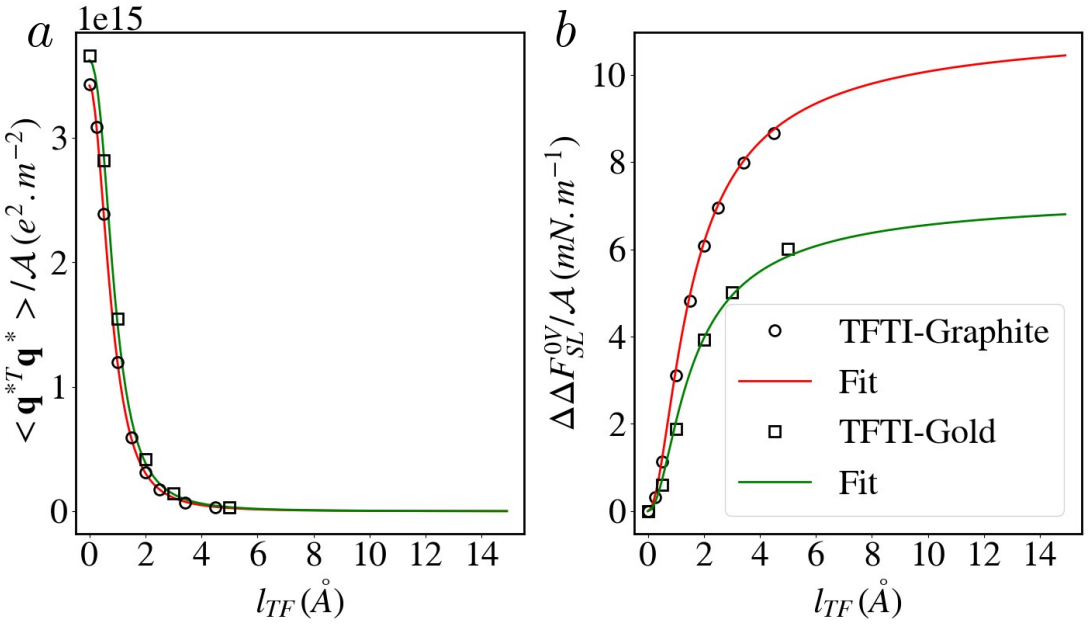

FIG. 9: Thomas-Fermi Thermodynamic Integration (TFTI): comparison between graphite and gold. (a) Average sum of the square of the atomic electrode charges, per unit area, as a function of l_{TF}. (b) Free energy difference per unit area, at 0 V, $\Delta\Delta F_{SL}^{0V}(l_{TF})/\mathcal{A}$. Both panels compare results for the graphite-1M NaCl cell (open circles and red lines – snapshot in figure 2d of the main text) and the gold-1M NaCl cell (open squares and green lines – snapshot in figure 3 of the main text). The solid lines are fits of the form Eq. 13 of the main text for panel a (and corresponding for b), with parameters adjusted on the simulation data of panel a.

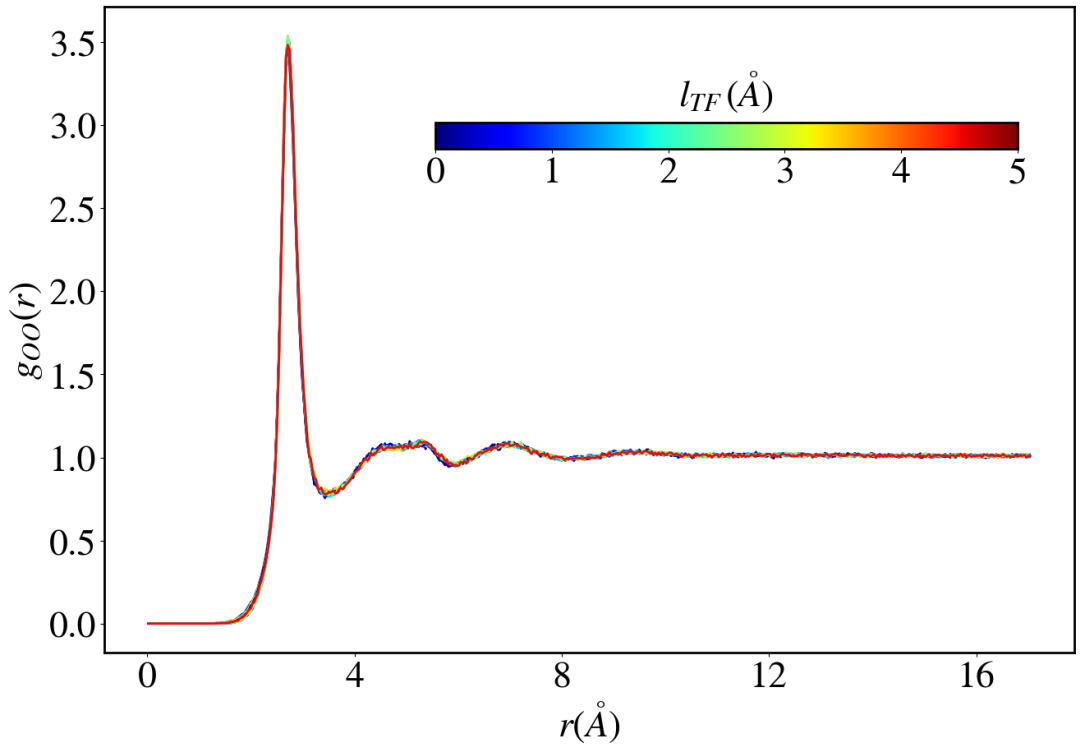

FIG. 10: Lateral correlations between water molecules in the first layer adsorbed on each electrode in a 1M NaCl / graphite capacitor at $\Delta\Psi = 0$ V. The figure shows the 2D radial distribution function of oxygen atoms, for a range of l_{TF} indicated by the color bar. All curves are superimposed.

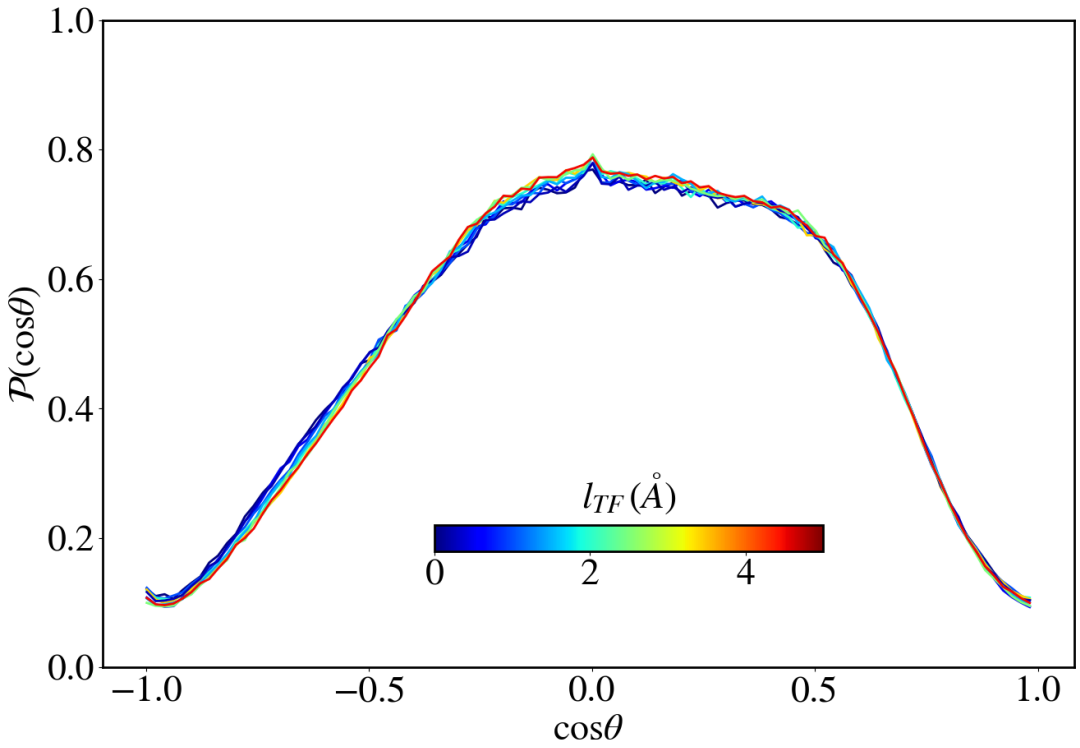

FIG. 11: Orientation of water molecules in the first layer adsorbed on each electrode in a 1M NaCl / graphite capacitor at $\Delta\Psi = 0$ V. The figure shows the distribution of $\cos\theta$, with θ the angle between the molecular dipole and the outward normal to the electrode surfaces, for a range of l_{TF} indicated by the color bar.

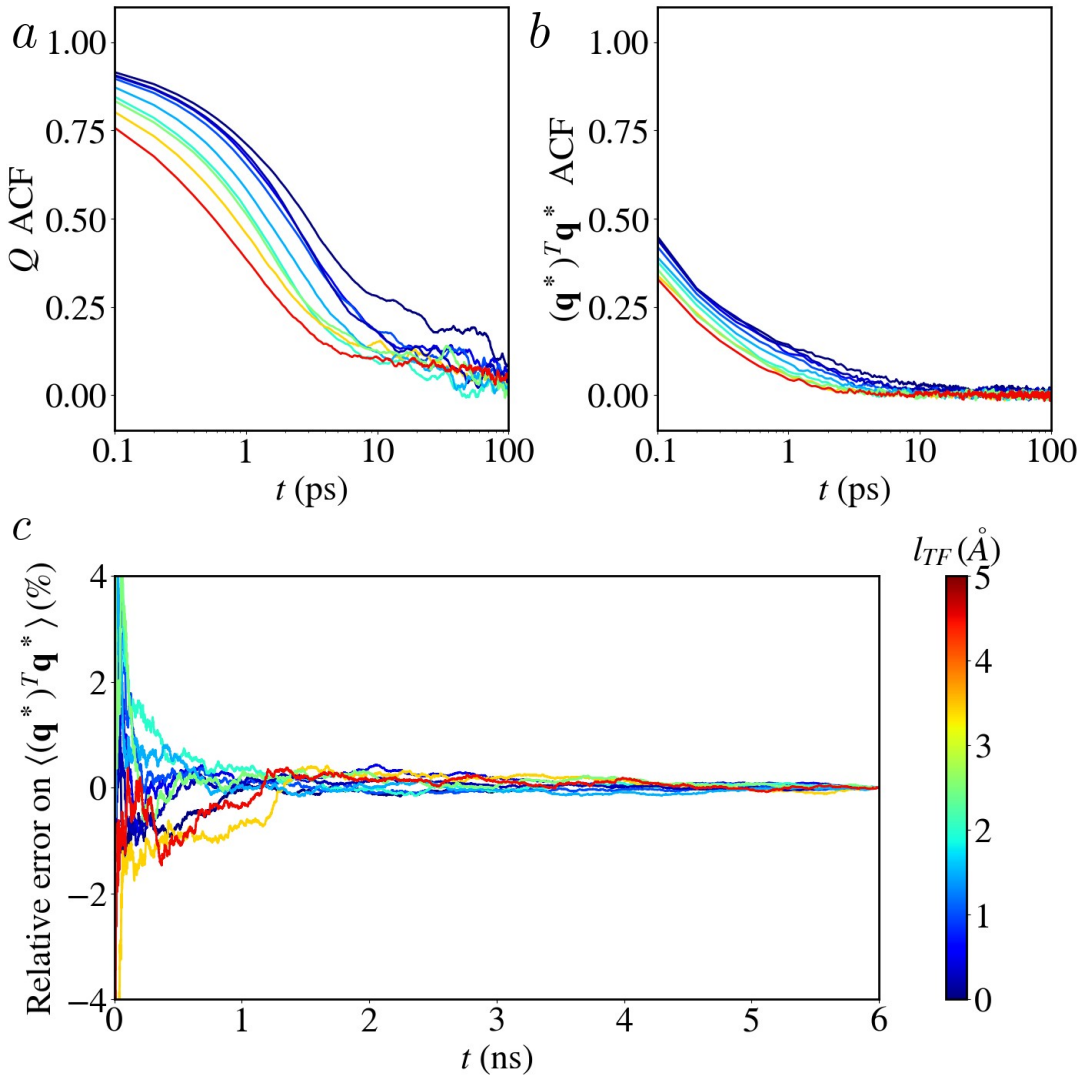

FIG. 12: Effect of l_{TF} on dynamical properties and the convergence of averages. Normalized autocorrelation function (ACF), defined as $C(t) = \langle A(0)A(t)\rangle / \langle A^2\rangle$, of the total charge $A = Q$ (a) and of the sum of the squared charges $A = (\mathbf{q}^*)^T\mathbf{q}^*$ (b). (c) Evolution of the relative error $\left[\left\langle(\mathbf{q}^*)^T\mathbf{q}^*\right\rangle_t - \left\langle(\mathbf{q}^*)^T\mathbf{q}^*\right\rangle_\infty\right] / \left\langle(\mathbf{q}^*)^T\mathbf{q}^*\right\rangle_\infty$ as a function of the trajectory length t (the error is computed relative to the largest simulation time $t_\infty = 6$ ns). All results are shown for a 1M NaCl / graphite capacitor at $\Delta\Psi = 0$ V, for a range of l_{TF} indicated by the color bar.

[1] F. Mugele and J.-C. Baret, Journal of Physics: Condensed Matter, 2005, **17**, R705–R774.
[2] C. D. Daub, D. Bratko, K. Leung and A. Luzar, J. Phys. Chem. C, 2007, **111**, 505–509.
[3] J. R. Choudhuri, D. Vanzo, P. A. Madden, M. Salanne, D. Bratko and A. Luzar, ACS Nano, 2016, **10**, 8536–8544.
[4] J. Sweeney, F. Hausen, R. Hayes, G. B. Webber, F. Endres, M. W. Rutland, R. Bennewitz and R. Atkin, Phys. Rev. Lett., 2012, **109**, 155502.
[5] H. Li, R. J. Wood, M. W. Rutland and R. Atkin, Chemical Communications, 2014, **50**, 4368–4370.
[6] O. Y. Fajardo, F. Bresme, A. A. Kornyshev and M. Urbakh, Sci. Rep., 2015, **5**, 7698.
[7] O. Y. Fajardo, F. Bresme, A. A. Kornyshev and M. Urbakh, J. Phys. Chem. Lett., 2015, **6**, 3998.
[8] K. Pivnic, F. Bresme, A. A. Kornyshev and M. Urbakh, ACS Applied Nano Materials, 2020.
[9] C. S. Perez-Martinez and S. Perkin, Soft Matter, 2019, **15**, 4255–4265.
[10] M. Li, M. N. Idros, Y. Wu, T. Burdyny, S. Garg, X. S. Zhao, G. Wang and T. E. Rufford, Journal of Materials Chemistry A, 2021, **9**, 19369–19409.
[11] Y. Montelongo, D. Sikdar, Y. Ma, A. J. S. McIntosh, L. Velleman, A. R. Kucernak, J. B. Edel and A. A. Kornyshev, Nature Materials, 2017, **16**, 1127–1135.
[12] J. Comtet, A. Niguès, V. Kaiser, B. Coasne, L. Bocquet and A. Siria, Nat. Mater., 2017, **16**, 634–639.
[13] A. Lainé, A. Niguès, L. Bocquet and A. Siria, Physical Review X, 2020, **10**, 011068.
[14] L. Garcia, L. Jacquot, E. Charlaix and B. Cross, Faraday Discussions, 2017, **206**, 443–457.
[15] R. R. Netz, Physical Review E, 1999, **60**, 3174–3182.
[16] A. Arnold, K. Breitsprecher, F. Fahrenberger, S. Kesselheim, O. Lenz and C. Holm, Entropy, 2013, **15**, 4569–4588.
[17] K. Breitsprecher, K. Szuttor and C. Holm, J. Phys. Chem. C, 2015, **119**, 22445–22451.
[18] A. A. Kornyshev, N. B. Luque and W. Schmickler, J. Solid State Electrochem., 2014, **18**, 1345–1349.
[19] A. A. Lee and S. Perkin, J. Phys. Chem. Lett., 2016, **7**, 2753.
[20] N. Ashcroft and N. Mermin, Solid State Physics, Holt, Rinehart and Winston, 1976.
[21] N. D. Lang and W. Kohn, Physical Review B, 1971, **3**, 1215–1223.
[22] A. Kornyshev and M. Vorotyntsev, Surface Science, 1980, **101**, 23–48.
[23] A. A. Kornyshev, W. Schmickler and M. A. Vorotyntsev, Phys. Rev. B, 1982, **25**, 5244–5256.
[24] C. C. Rochester, A. A. Lee, G. Pruessner and A. A. Kornyshev, ChemPhysChem, 2013, **14**, 4121–4125.
[25] V. Kaiser, J. Comtet, A. Niguès, A. Siria, B. Coasne and L. Bocquet, Faraday Discuss., 2017, **199**, 129–158.
[26] N. Bonnet, T. Morishita, O. Sugino and M. Otani, Phys. Rev. Lett., 2012, **109**, 266101.
[27] F. Deißenbeck, C. Freysoldt, M. Todorova, J. Neugebauer and S. Wippermann, Physical Review Letters, 2021, **126**, 136803.
[28] J. Lan, J. Hutter and M. Iannuzzi, The Journal of Physical Chemistry C, 2018, **122**, 24068–24076.
[29] J. Lan, V. V. Rybkin and M. Iannuzzi, The Journal of Physical Chemistry Letters, 2020, **11**, 3724–3730.
[30] S. Sakong and A. Groß, Physical Chemistry Chemical Physics, 2020, **22**, 10431–10437.
[31] J.-B. Le, A. Chen, L. Li, J.-F. Xiong, J. Lan, Y.-P. Liu, M. Iannuzzi and J. Cheng, JACS Au, 2021, **1**, 569–577.
[32] P. Li, J. Huang, Y. Hu and S. Chen, The Journal of Physical Chemistry C, 2021, **125**, 3972–3979.
[33] J. I. Siepmann and M. Sprik, J. Chem. Phys., 1995, **102**, 511–524.
[34] S. K. Reed, O. J. Lanning and P. A. Madden, J. Chem. Phys., 2007, **126**, 084704.
[35] D. T. Limmer, C. Merlet, M. Salanne, D. Chandler, P. A. Madden, R. van Roij and B. Rotenberg, Phys. Rev. Lett., 2013, **111**, 106102.
[36] L. Scalfi, D. T. Limmer, A. Coretti, S. Bonella, P. A. Madden, M. Salanne and B. Rotenberg, Phys. Chem. Chem. Phys., 2020, **22**, 10480–10489.
[37] A. P. Willard, S. K. Reed, P. A. Madden and D. Chandler, Faraday Discuss., 2009, **141**, 423–441.
[38] C. Merlet, B. Rotenberg, P. A. Madden and M. Salanne, Phys. Chem. Chem. Phys., 2013, **15**, 15781–15792.
[39] M. A. Pounds, M. Salanne and P. A. Madden, Mol. Phys., 2015, **113**, 2451–2462.
[40] D. T. Limmer, A. P. Willard, P. Madden and D. Chandler, Proc. Natl. Acad. Sci. U.S.A., 2013, **110**, 4200–4205.
[41] A. P. Willard, D. T. Limmer, P. A. Madden and D. Chandler, J. Chem. Phys., 2013, **138**, 184702.
[42] D. T. Limmer, A. P. Willard, P. A. Madden and D. Chandler, J. Phys. Chem. C, 2015, **119**, 24016–24024.
[43] J. A. Kattirtzi, D. T. Limmer and A. P. Willard, Proc. Natl. Acad. Sci. U.S.A., 2017, **114**, 13374–13379.
[44] C. Merlet, D. T. Limmer, M. Salanne, R. van Roij, P. A. Madden, D. Chandler and B. Rotenberg, J. Phys. Chem. C, 2014, **118**, 18291–18298.
[45] B. Rotenberg and M. Salanne, J. Phys. Chem. Lett., 2015, **6**, 4978–4985.
[46] M. V. Fedorov and A. A. Kornyshev, Chem. Rev., 2014, **114**, 2978—3036.
[47] L. Scalfi, M. Salanne and B. Rotenberg, Annual Review of Physical Chemistry, 2021, **72**, 189.
[48] C. Y. Son and Z.-G. Wang, Proceedings of the National Academy of Sciences, 2021, **118**, e2020615118.
[49] C. Merlet, C. Péan, B. Rotenberg, P. A. Madden, P. Simon and M. Salanne, J. Phys. Chem. Lett., 2013, **4**, 264–268.
[50] S. Ntim and M. Sulpizi, Phys. Chem. Chem. Phys., 2020, **22**, 10786–10791.
[51] L. Scalfi, T. Dufils, K. G. Reeves, B. Rotenberg and M. Salanne, The Journal of Chemical Physics, 2020, **153**, 174704.
[52] A. Schlaich, D. Jin, L. Bocquet and B. Coasne, Nature Materials, 2021, 1–9.
[53] T. R. Gingrich and M. Wilson, Chem. Phys. Lett., 2010, **500**, 178–183.
[54] E. Paek, A. J. Pak and G. S. Hwang, The Journal of Chemical Physics, 2015, **142**, 024701.
[55] R. Evans and U. Marini Bettolo Marconi, The Journal of Chemical Physics, 1987, **86**, 7138–7148.

[56] L. Scalfi, B. Coasne and B. Rotenberg, The Journal of Chemical Physics, 2021, **154**, 114711.
[57] O. Magnussen, Chem. Rev., 2002, **102**, 679–726.
[58] O. M. Magnussen and A. Groß, J. Am. Chem. Soc., 2019, **141**, 4777–4790.
[59] P. Clabaut, B. Schweitzer, A. W. Götz, C. Michel and S. N. Steinmann, Journal of Chemical Theory and Computation, 2020, **16**, 6539–6549.
[60] S. Gim, K. J. Cho, H.-K. Lim and H. Kim, Scientific Reports, 2019, **9**, 14805.
[61] K. J. Cho, S. Gim, H.-K. Lim, C. Kim and H. Kim, The Journal of Physical Chemistry C, 2020, **124**, 11392–11400.
[62] J. Oshiki, H. Nakano and H. Sato, The Journal of Chemical Physics, 2021, **154**, 144107.
[63] A. Serva, L. Scalfi, B. Rotenberg and M. Salanne, The Journal of Chemical Physics, 2021, **155**, 044703.
[64] Y. Xie, L. Fu, T. Niehaus and L. Joly, Physical Review Letters, 2020, **125**, 014501.
[65] M. Salanne, B. Rotenberg, K. Naoi, K. Kaneko, P.-L. Taberna, C. P. Grey, B. Dunn and P. Simon, Nature Energy, 2016, **1**, 16070.
[66] M. D. Boamah, E. H. Lozier, J. Kim, P. E. Ohno, C. E. Walker, T. F. Miller and F. M. Geiger, Proceedings of the National Academy of Sciences, 2019, **116**, 16210–16215.
[67] A. Siria, M.-L. Bocquet and L. Bocquet, Nat Rev Chem, 2017, **1**, 0091.
[68] M. Simoncelli, N. Ganfoud, A. Sene, M. Haefele, B. Daffos, P.-L. Taberna, M. Salanne, P. Simon and B. Rotenberg, Physical Review X, 2018, **8**, 021024.
[69] A. Marin-Laflèche, M. Haefele, L. Scalfi, A. Coretti, T. Dufils, G. Jeanmairet, S. K. Reed, A. Serva, R. Berthin, C. Bacon, S. Bonella, B. Rotenberg, P. A. Madden and M. Salanne, Journal of Open Source Software, 2020, **5**, 2373.
[70] L. Scalfi and B. Rotenberg, Data for "Microscopic origin of the effect of substrate metallicity on interfacial free energies", 2021, `https://doi.org/10.5281/zenodo.5658485`.
[71] H. J. C. Berendsen, J. R. Grigera and T. P. Straatsma, J. Phys. Chem., 1987, **91**, 6269–6271.
[72] L. X. Dang, J. Am. Chem. Soc., 1995, **117**, 6954–6960.
[73] T. Werder, J. H. Walther, R. L. Jaffe, T. Halicioglu and P. Koumoutsakos, J. Phys. Chem. B, 2003, **107**, 1345–1352.
[74] A. Berg, C. Peter and K. Johnston, Journal of Chemical Theory and Computation, 2017, **13**, 5610–5623.